Los Alamos National Laboratory is operated by the University of California for the United States Department of Energy under contract W-7405-ENG-36.

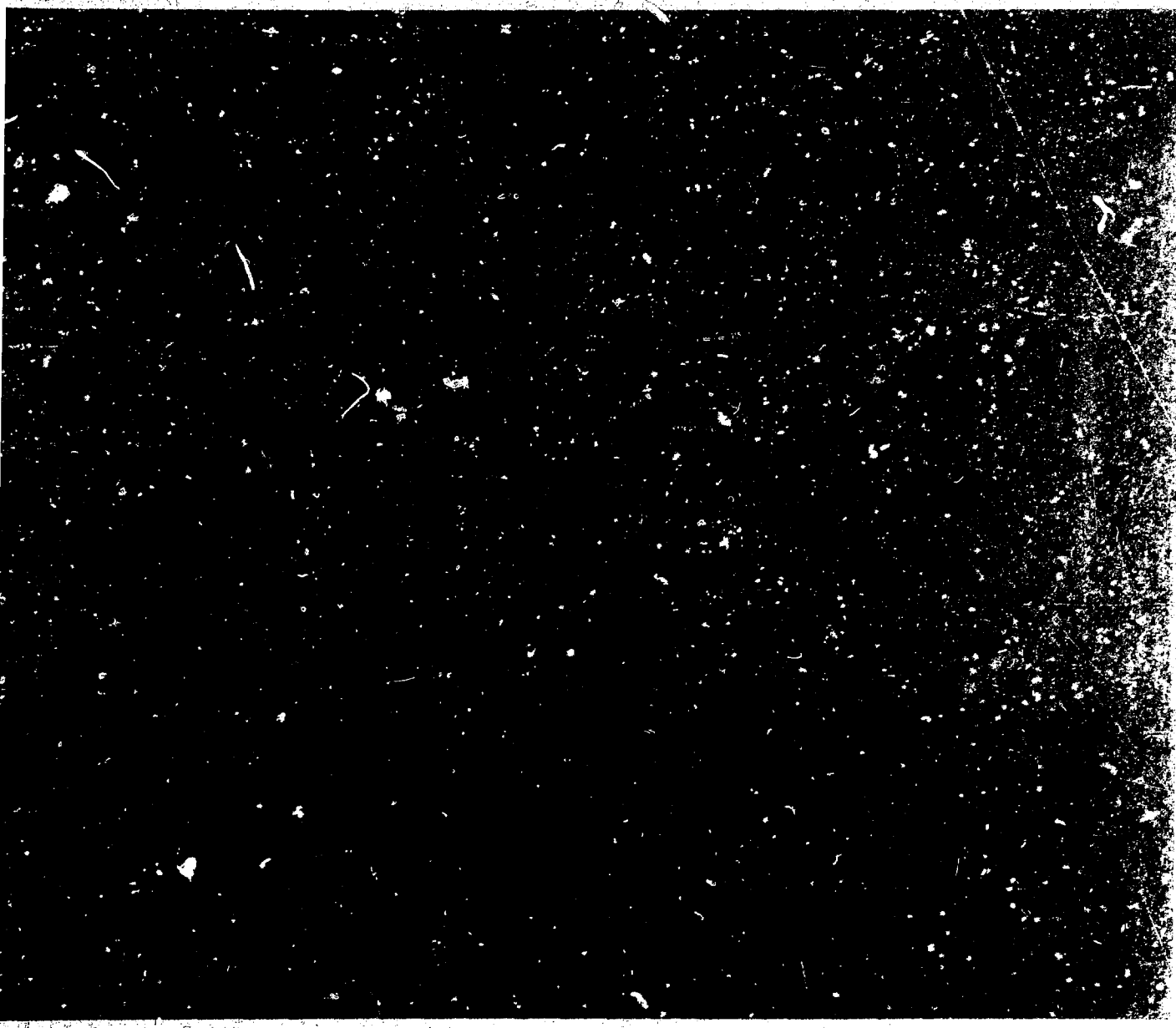

Los Alamos Los Alamos National Laboratory
Los Alamos, New Mexico 87545

LA-8937-T
Thesis

UC-34c
Issued: August 1981

Inclusive Proton Spectra and Total Reaction Cross Sections for Proton-Nucleus Scattering at 800 MeV

John Alexander McGill

Los Alamos National Laboratory
Los Alamos, New Mexico 87545

TABLE OF CONTENTS

INCLUSIVE PROTON SPECTRA AND TOTAL REACTION CROSS SECTIONS FOR PROTON-NUCLEUS SCATTERING AT 800 MeV

by

John Alexander McGill

ABSTRACT

Current applications of multiple scattering theory to describe the elastic scattering of medium energy protons from nuclei have been shown to be quite successful in reproducing the experimental cross sections. These calculations use the impulse approximation, wherein the scattering from individual nucleons in the nucleus is described by the scatering amplitude for a free nucleon. Such an approximation restricts the inelastic channels to those initiated by nucleon-nucleon scattering.

As a first step in determining the nature of p + nucleus scattering at 800 MeV, both total reaction cross sections and (p,p′) inclusive cross sections were measured and compared to the free p + p cross sections. We conclude that as much as 85 % of all reactions in a nucleus proceed from interactions with a single nucleon in the nucleus, and that the impulse approximation is a good starting point for a microscopic descripton of p + nucleus interactions at 800 MeV.

CHAPTER I

INTRODUCTION

The internucleon spacing in nuclear matter is about 1.3 fm, and the deBroglie wavelength of an 800 MeV proton is 1.5 fm. This information suggests that 800 MeV p + nucleus elastic scattering data should be sensitive to the one-body density of the target nucleus; several multiple scattering theories[1-4] attempt to describe quantitatively the scattering process in terms of the fundamental proton-nucleon interactions.

Current multiple scattering theory is an outgrowth of earlier attempts to explain the scattering of elementary particles from complex nuclei. Due to the partial transparency of the nucleus to low energy neutrons, a theory was developed[5] which considered the projectile as incident on a sphere of material characterized by an absorption coefficient and an index of refraction. Such an "optical" model provides good agreement with data for projectiles whose wavelength is significantly longer than the internucleon distances.

For projectiles having wavelengths shorter than internucleon spacings, the earliest attempt to obtain a microscopic theory of scattering resulted in the Impulse Approximation of Chew[6,7]. The assumptions under which the model is valid are that the scattering takes place on a single nucleon, and that the distortion and binding effects of the nuclear medium are negligible. Binding corrections and

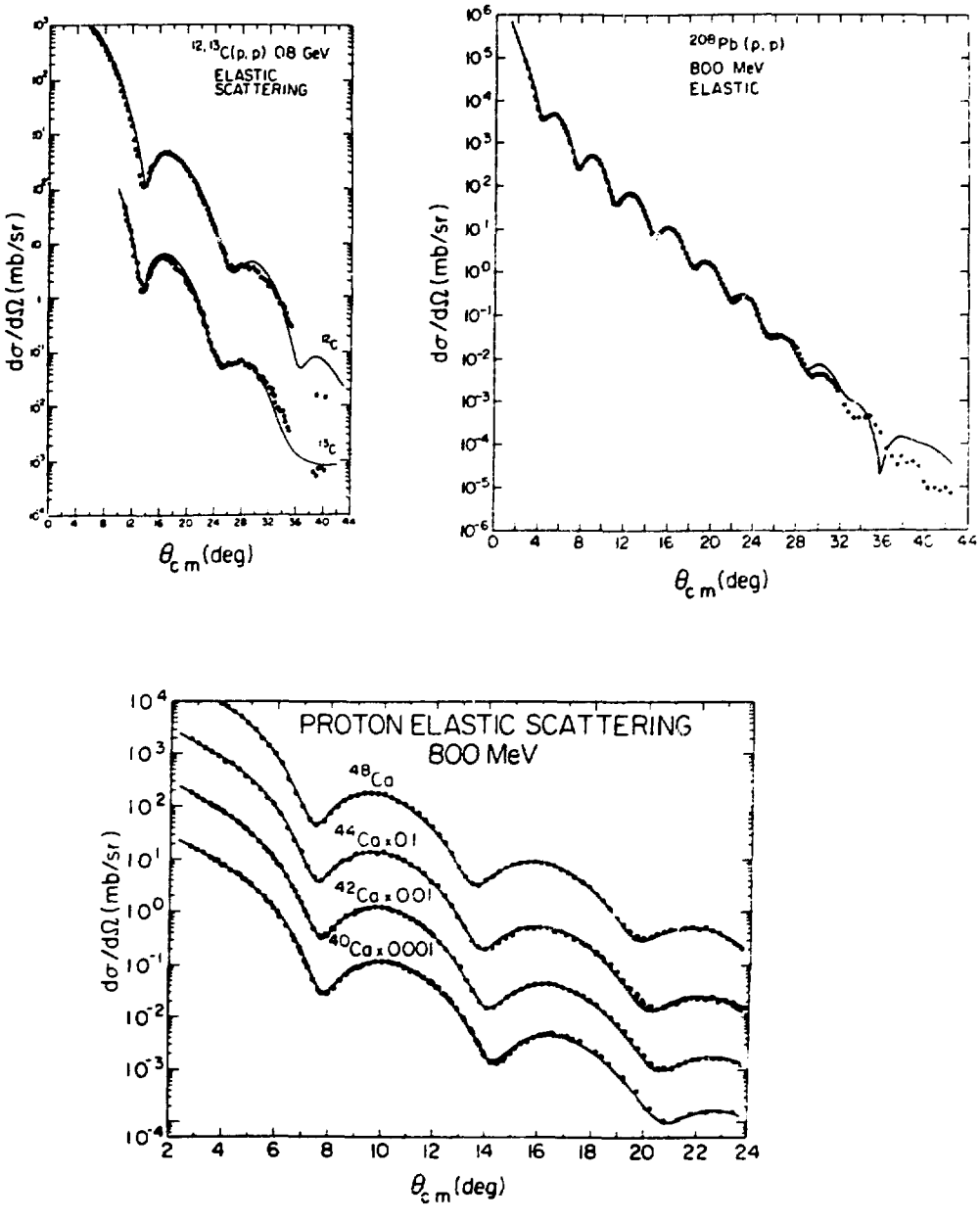

Figure 1.1: Differential cross sections for 800 MeV proton scattering from (a.) $^{12,13}C$, (b.) ^{208}Pb, and (c.) $^{40,42,44,48}Ca$. The curves are those obtained with the microscopic optical potential of KMT.

multiple scattering terms were later introduced as refinements to the theory.

Watson[1-3] married the optical model with the impulse approximation, showing rigorously how to construct an optical potential from the single scattering amplitudes. Such a construction provided the theoretical justification for the use of an optical potential calculated from nucleon-nucleon scattering amplitudes and the ground state density distribution. Kerman, McManus, and Thaler[8] reformulated the Watson expansion in a form more readily suited to the use of "free" nucleon-nucleon amplitudes. Figure 1.1 shows the success of the KMT theory in describing 800 MeV p + nucleus elastic scattering from various nuclei[13,23,25].

Both the KMT and Watson Multiple Scattering theories solve the Schrödinger equation in integral form

$$\Psi^+ = \Phi + GV\underline{A}\Psi^+ \quad , \tag{1.1}$$

where $\underline{A}$ projects out antisymmetrized states and

$$G = (E - H_O - H_A + i\varepsilon)^{-1} \quad ,$$

by defining a scattering matrix T such that

$$T\Phi = V\Psi^+ \quad . \tag{1.2}$$

With this definition Equation 1.1 becomes

$$T = V + VG\underline{A}T \quad . \tag{1.3}$$

The KMT approach involves defining a single scattering operator

$$\hat{t}_i = v_i + v_i G\underline{A}\hat{t}_i \tag{1.4}$$

where $\hat{t}_i$ is the amplitude for scattering from the i^{th} nucleon, then v_i is defined such that

$$\sum_{i=1}^{A} v_i = Av = V \quad . \tag{1.5}$$

Using the definitions in Equations 1.4 and 1.5 in 1.3, and iterating 1.3, gives

$$T = A\hat{t} + (A-1)\hat{t}G\underline{A}T \quad . \tag{1.6}$$

To cast the problem in a proper Lippmann-Schwinger form, the auxiliary operator T′ is defined

$$T' = \frac{A-1}{A} T \tag{1.7}$$

so that Equation (1.6) becomes

$$T' = (A-1)\hat{t} + (A-1)\hat{t}G\underline{A}T' \quad . \tag{1.8}$$

From Equation (1.3) it is desired to provide an optical potential U such that

$$T = U + UGPT \tag{1.9}$$

where the operator P projects out the elastic states only, and its complementary operator Q projects out only inelastic states. Of course

$$P + Q = A \quad . \tag{1.10}$$

With T′ as given in Equation (1.8) the corresponding requirement for the optical potential is

$$T' = U' + U'PGT' \quad . \tag{1.11}$$

Solving Equation (1.8) for T′ and substituting into (1.11) gives

$$U' = (A-1)\hat{t} + (A-1)U'G\hat{Q}\hat{t} \quad . \tag{1.12}$$

The treatment up to this point is exact, and if the microscopic single scattering amplitudes defined in Equation 1.4 were known, the optical potential could be constructed. Unfortunately these amplitudes which describe the proton-nucleon interaction in nuclear matter are not known, and practical calculations approximate these amplitudes with free nucleon-nucleon amplitudes, and the series in (1.12) is truncated at some point. The use of free p + p and p + n amplitudes in place of

$\hat{t}$ constitutes the impulse approximation in the context of multiple scattering theory.

One important consequence of the use of the impulse approximation is that, within the context of the theory, all reactions must evolve from quasi-free doorways[9-11]. In other words only quasi-elastic and quasi-free pion production mechanisms are allowed to initiate the process leading to reactions. Clearly unless these two processes account for a substantial portion of the physical reaction cross section, the theory will be inadequate.

As a first step in determining the nature of the 800 MeV p + nucleus reaction mechanism, both total reaction cross sections and (p,p′) inclusive spectra at forward angles were measured.

Chapter II describes the experiments, while Chapter III contains a description of the data analysis. Finally Chapter IV contains a comparison of the total reaction cross sections with angle-integrated inclusive (p,p′) cross sections, and with predictions given by KMT calculations[35].

We tentatively conclude that two-nucleon processes account for about 80% of the 800 MeV p + nucleus total reaction cross section, and that the impulse approximation appears to be a good starting point for microscopic calculations of p + nucleus observables at 800 MeV.

CHAPTER II

EXPERIMENTAL ARRANGEMENT

Both experiments were done using the High Resolution Spectrometer at the Los Alamos Meson Physics Facility. A brief description of the beam line and spectrometer system is given in Section A; Experiment 470 "Reactive Content of the Optical Potential" is fully described in Section B; and Section C describes Experiment 386 "Total Reaction Cross Sections for p + Nuclei".

A. BEAM LINE AND SPECTROMETER

The LAMPF LINAC has been extensively described elsewhere[12]. Briefly, both H^+ and H^- ions are accelerated to 750 keV by separate Cockroft-Walton injectors at which point they are passed to the second stage or Alvarez section (drift tube), where they are accelerated to 100 MeV. The third stage, the side-coupled cavity section, then accelerates the ions to 800 MeV.

Once the final velocity of 0.84c has been reached, the H^+ and H^- beams are separated by a dipole magnet and each proceeds to different experimental areas. Line A takes the H^+ to several meson production targets, thence to a beam dump. Line X accepts the H^- beam wherein it is focussed and steered onto a stripper. At the stripper a fraction of the H^- ions are relieved of their electrons then bent via a dipole into Line C (see Figure 2.1). The unstripped H^- continues to other experimental areas.

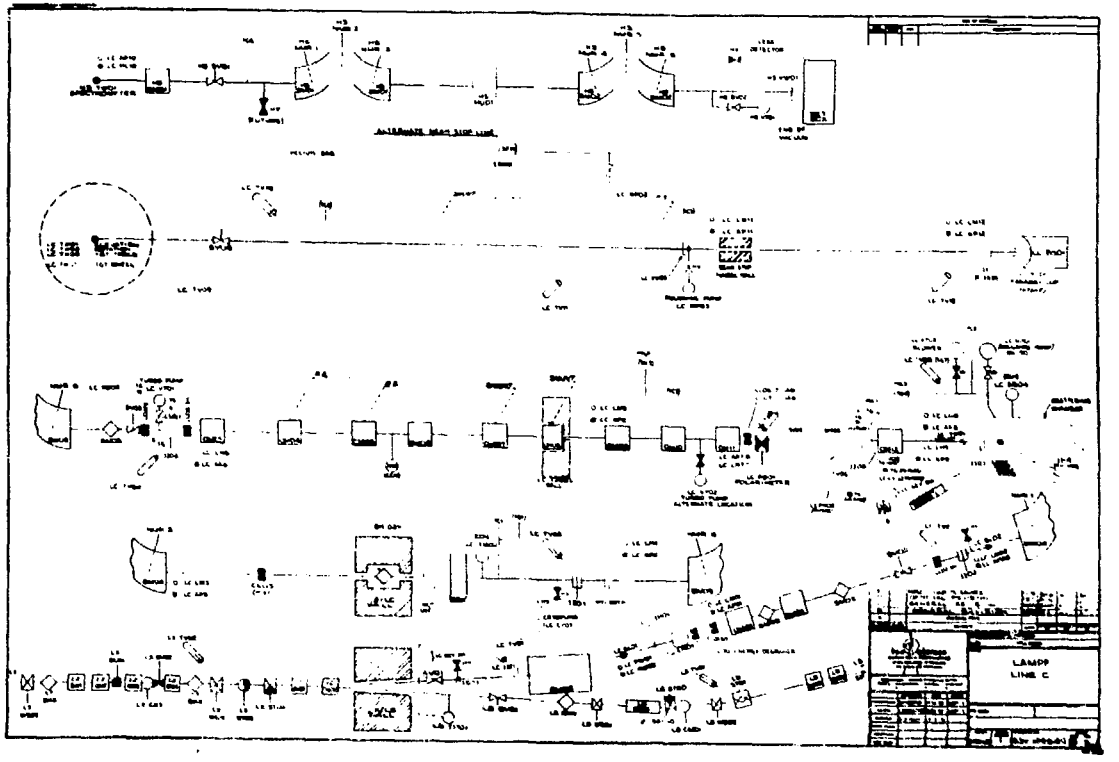

Figure 2.1: A schematic drawing of the major beam-line components in Line C.

Blanpied has given a good description of the Line C beam optics[13]. The beam line basically consists of three sections: dispersion, twister, and matching. The beam is dispersed in the horizontal plane by a pair of dipole magnets. Beam phase space is then rotated 90^{o} by a set of five quadrupoles. Additional quadrupoles are then used to provide a beam on target whose dispersion is matched to that of the HRS for operation in the energy-loss mode.

The HRS is a Quadrupole-Dipole-Dipole (QDD) system mounted in a vertical plane[14]. The optics provide parallel-to-point focussing in the non-dispersion direction ($\hat{y}$) and point-to-point focussing in the dispersion ($\hat{x}$) direction. Proper dispersion matching between the line C optics and the HRS optics ensures that (apart from the kinematical $\frac{dE}{d\theta}$) all scattered particles having the same energy loss at the target will be focussed at the same transverse coordinate ($\hat{x}$) on the focal plane. For a narrow beam in the $\hat{y}$ direction, the focal plane coordinate in the non-dispersion ($\hat{y}$) direction is proportional to the scattering angle.

A schematic of the HRS focal plane detection system is shown in Figure 2.2. Counters C1 through C6 are delay-line (DL) and drift chambers (DC's) which provide position and angle information; S1-S4 are scintillators which give pulse height and time-of-flight information, and provide the "event" trigger. The detection system is designed for a wide variety of purposes and only portions of it were used in these experiments.

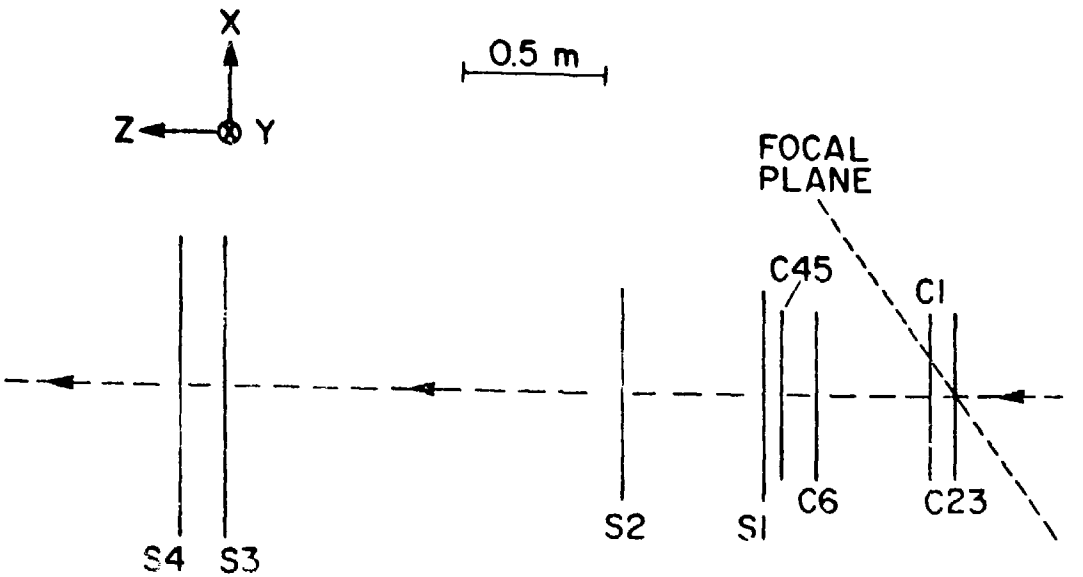

Figure 2.2: The HRS focal plane detection system. S1-S4 are scintillators; C1-C6 are wire chambers.

The four scintillators are optically coupled to EMI 9oi3B photomultiplier tubes at each end. The physical characteristics of the scintillators are listed in Table 2.1. The anode signal from each photomultiplier is input to an LRS 621 leading edge discriminator. For each scintillator, the two discriminator signals (top and bottom) are fed into an LRS 624 Meantimer, the output of which is a signal whose arrival time is independent of position in the scintillator. Normally the meantimed signals are used to form a four-fold coincidence, so that a good event is defined by the requirement of S1•S2•S3•S4. This constitutes the HRS event trigger, alerting other electronics modules in the system that a good event (i.e. not a random charged particle from room background) has occured and other data, e.g. chamber information, may be read in.

Another function of the focal plane scintillators is the identification of particle types at the focal plane. For a given field setting the HRS will transport to the focal plane different particle types with the same value of p/q, where p is the particle momentum and q is its charge. Field settings coresponding to an 800 MeV proton (p/q = 1463 MeV/c•e) also transmit a 500 MeV deuteron, a 350 MeV triton, a 700 MeV ^{3}He, and a 1330 MeV π^{+}. Therefore some scheme of particle identification (PID) at the focal plane is necessary. The HRS system provides PID through measuring time of flight between two scintillators, and pulse height in one scintillator. Time of flight goes like $\frac{l}{v}$, or $\frac{E}{p}$. Pulse height from a scintillator is a function of

Detector	Material	Size(cm)	Distance from Focal Plane(cm)
S1	Pilot B	76.2 × 1.27 × 0.64	68.6
S2	Pilot F	77.5 × 10.8 × 0.64	119.4
S3	NE110	106.7 × 14.0 × 0.95	259.1
S4	NE110	106.7 × 14.0 × 0.95	274.3

Table 2.1 : Specifications of event scintillator geometries used in Experiment 470.

the energy lost in the scintillator, which is proportional to $\frac{qE}{p}^2$. Thus particles having different masses or charges can be distinguished.

In Figure 2.2 C1 and C6 are "delay" (D) chambers which provide information redundant to C2-C5, "drift" chambers. Consequently C1 and C6 were not used in this experiment. Each of the four drift chambers used contains a pair of planes for $\hat{x}$ information, and a pair for $\hat{y}$ information. The design and construction of these detectors has been discussed extensively in the literature[15,16], and only a qualitative description is given here.

A schematic representation of a plane is shown in Figure 2.3. Alternating anode and cathode wires are spaced 4 mm apart, with anode wires attached at regular intervals to a delay line, and cathode wires bussed together and grounded. Each physical unit (stacked $\hat{x}$-plane, $\hat{y}$-plane, $\hat{x}$-plane, $\hat{y}$-plane) is covered with .001" aluminized Mylar. A mixture of Argon, CO_2, methylal, and isobutane in the chamber serves as an ionizing medium; i.e., a charged particle traversing a plane will produce ion-electron pairs which are accelerated to their respective wires. Electrons in the vicinity of the anode will cascade, providing a signal on the order of a few millivolts which passes in both directions down the delay line. The arrival times of these signals are

$$t_1 = t_d + n\,\Delta t \quad ,$$

where t_d is the drift time in the gas, n is the number of wire

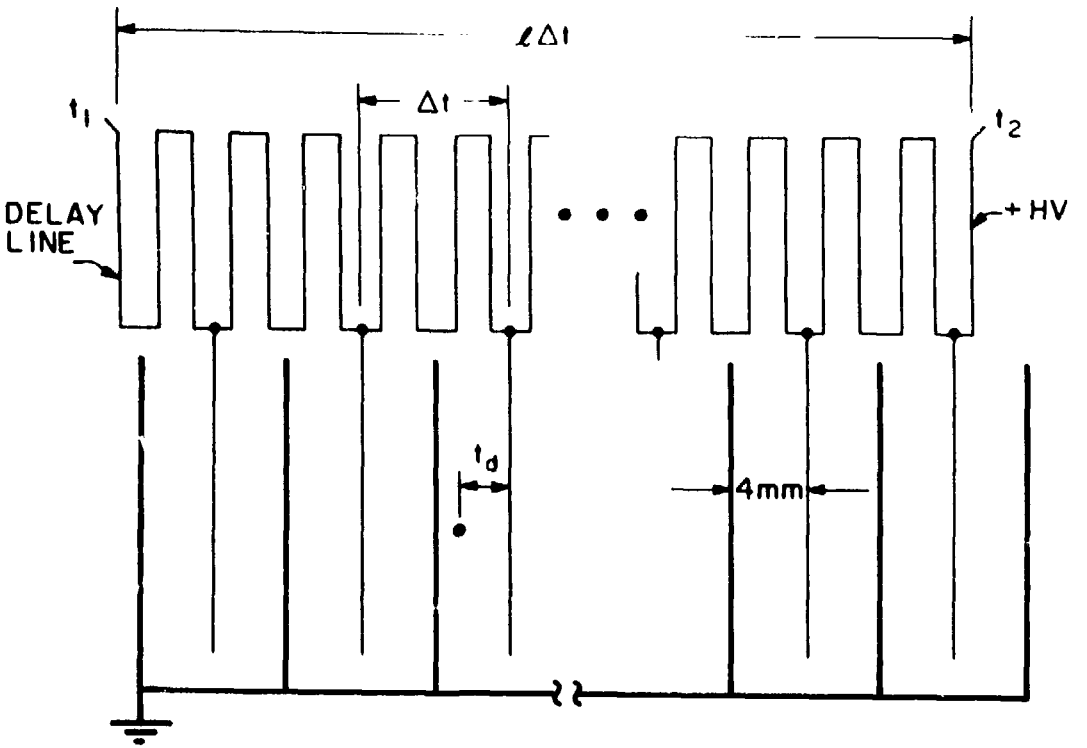

Figure 2.3: Schematic drawing of an anode plane in the drift chambers. Anode wires (thin lines) and cathode wires (thick lines) are separated by ~ 4 mm.

intervals between the left edge and the event wire, and Δt is the delay interval of each wire space; and

$$t_2 = t_d + (\ell - n)\ \Delta t \quad ,$$

where ℓ is the total number of wire intervals between the left and right edges. The time difference

$$t_1 - t_2 = 2n\Delta t - \ell\Delta t$$

reveals the event wire, while the time sum

$$t_1 + t_2 = 2t_d + \ell\Delta t$$

yields the drift time t_d. In both quantities the constant $\ell\Delta t$ can be treated as an offset and removed either in hardware with appropriate delays, or in software. Thus the time difference locates the event to ± 4 mm, and the time sum is used to interpolate from there. Figure 2.4a is a spectrum of time difference showing discrete wire positions; Figure 2.4b shows a drift spectrum of $t_1 + t_2$. These data were taken by illuminating the focal plane uniformly. Note that a constant drift velocity would result in a flat drift spectrum out to 4 mm , and zero from there out. Nonlinearities as in Figure 2.4b are accomodated by generating a look-up table which gives the drift time to position conversion in increments of ~ 0.1 mm.

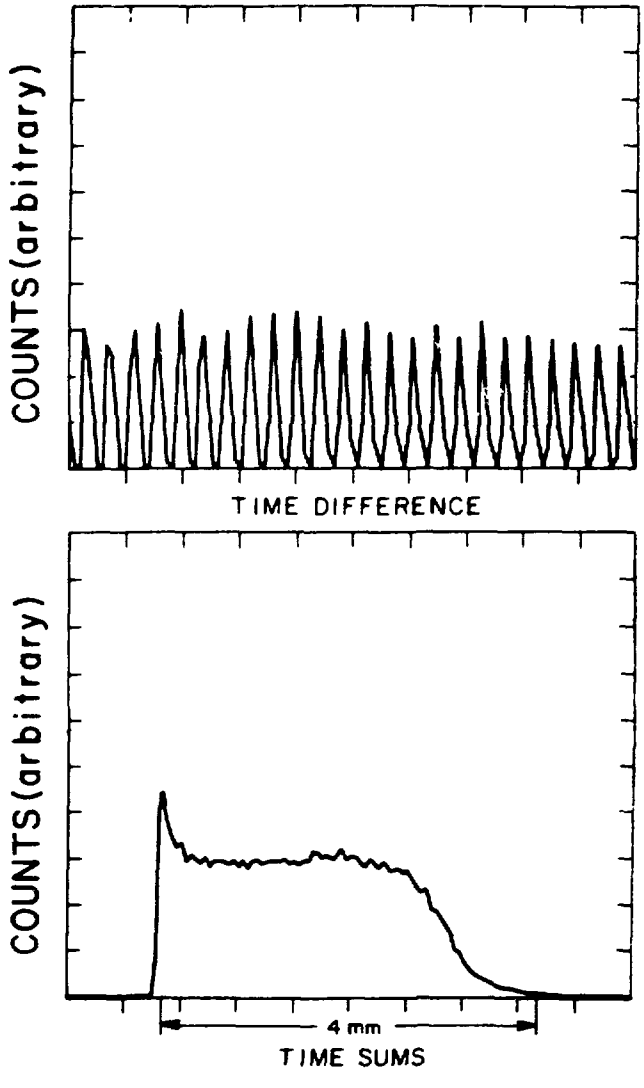

Figure 2.4: Histograms of the difference and sum of the arrival times of the signals from the left edge of an anode plane (t_1) and the right edge (t_2).

There is one ambiguity remaining in the location of the event: did the event occur to the left or the right of the anode? Here enters the reason for placing two x-y pairs in each physical unit. By locating the event to within this ambiguity in two planes which are offset by 4 mm, four possible combinations can be formed: (left,left), (left,right), (right,left), and (right,right). One of these combinations will minimize the difference between the two positions, and that one is chosen.

Once accurate positions in all chambers are known, it is a simple geometric problem to generate the variables of interest at the focal plane : $(x_f, y_f, \theta_f, \phi_f)$, where θ_f is the angle in the dispersion plane and ϕ_f is the angle in the non-dispersion plane. These four quantities along with the inverse transport matrix and dipole field settings are sufficient to determine the properties of the scattering event. In particular the quantity

$$\delta = \frac{p_o - p_{sp}}{p_{sp}}$$

yields the momentum of the event (p_o) relative to the spectrometer central momentum (p_{sp}), known from the field settings. The relationships between the quantities are given by

$$\begin{bmatrix} y_t \\ \theta_t \\ \varphi_t \\ \delta \end{bmatrix} = \begin{bmatrix} 0.00 & 0.00 & -0.0644 & 0.1906 \\ 0.7471 & -0.8125 & 0.0818 & 0.0007 \\ -0.0229 & 0.0409 & -5.0249 & -0.1654 \\ 0.0555 & 0.0002 & 0.00 & 0.00 \end{bmatrix} \begin{bmatrix} x_f \\ \theta_f \\ y_f \\ \varphi_f \end{bmatrix} + A$$

where the subscript t refers to the target coordinates, and f refers to focal plane coordinates. Higher order corrections are contained in A. From the above it can be seen that the major elements in the physical terms are $\langle y_t | \varphi_f \rangle$, $\langle \varphi_t | y_f \rangle$, and $\langle \delta | x_f \rangle$. Finally, from this last quantity the dispersion of the HRS is 18.02 cm/%.

The calculation of physical quantities in terms of focal plane information is done in software (see Chapter III). Thus the statement in the preceding paragraph that "once accurate positions in all chambers are known..." implies that the outputs of various electronic modules are passed to a computer for analysis. This is accomplished by CAMAC[17,18].

Raw scintillator and drift chamber signals are transmitted from the HRS focal plane to the Area C Counting House (CCH). There the HRS trigger (S1·S2·S3·S4) is made and used as the common start to CAMAC time-to-digital converters (TDC's). Discriminated chamber signals are used as stops to yield t_1 and t_2 discussed above. Signals from S2 and S3 are used as stops to give time-of-flight. Also raw S3 and S4 signals are fed to CAMAC analog-to-digital converters (ADC's) for the pulse-height information used in particle identification. The outputs of these CAMAC modules are 8-bit words which are written to magnetic

tape via a PDP-11/45 computer. A total of 38 data words, containing time and pulse height information, are written for each event.

B. EXPERIMENT 470: "REACTIVE CONTENT OF THE OPTICAL POTENTIAL"

This experiment took place in two parts because of scheduling and beam-quality considerations. During December 1979, a mechanical problem developed in the sliding vacuum seal of the HRS scattering chamber which was deemed irreparable until after the holiday season. So the scattering chamber was isolated from the upstream beam line vacuum and from the downstream spectrometer vacuum by .010" Mylar windows. To reduce multiple scattering effects the scattering chamber was purged with Helium. Of course this had devastating effects on the obtainable momentum resolution and rendered the facility unusable for many purposes. However the resolution requirements of Experiment 470 were no more than one in 10^3. Further, spurious scattering events associated with the Helium could be accomodated by re-taking a partial set of data at a later date with good vacuum. So the experiment ran for approximately 10 days in December 1979 (Cycle 25), and another 5 days in March 1980 (Cycle 26).

Figure 2.5 is a schematic drawing showing the major components of the experiment. Protons with 800 MeV kinetic energy entered the scattering chamber from Line C and scattered from the target. Only a small fraction of the beam was scattered ($\sim 10^{-4}$), with the majority continuing on to a beam current monitor, thence to the beam stop. The beam current monitor (IC) was an Ion Chamber consisting of several

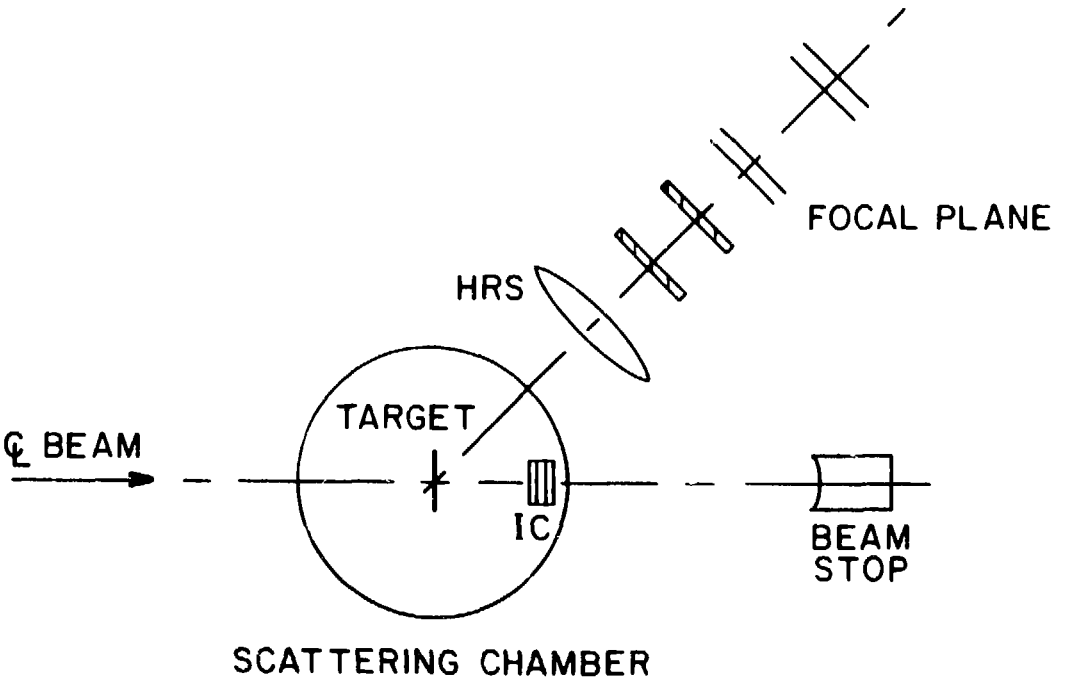

Figure 2.5: Schematic drawing of the experimental arrangement in Experiment 470.

conducting plates imbedded in a gas medium ($ArCO_2$), so that the plates collected the ionization current caused by the passage of a fast charged particle. This current was integrated, and the integral was written to tape for each run. Protons scattered from the target at the proper angle entered the HRS, where they were momentum analyzed and detected at the focal plane.

During Cycle 25 a target of liquid hydrogen was mounted in the HRS scattering chamber, and data were taken with the spectrometer at laboratory angles of 11°, 15°, 20°, 25°, and 30°. Upon completion of these data runs the cryogenic target was removed and targets of CH_2, CD_2, ^{12}C, ^{40}Ca, ^{90}Zr, and ^{208}Pb were mounted on the standard HRS target wheel. Data from these targets were taken at laboratory angles of 5°, 11°, 15°, and 20°. As stated earlier, all the Cycle 25 data were acquired with the scattering chamber full of Helium. A more or less complete set of data were taken with no target in the beam to gauge the effects of multiple scattering from the Helium.

In Cycle 26 targets of the same isotopes were mounted on the target wheel and data were taken at laboratory angles of 5°, 11°, and 20°. All these data were acquired with the scattering chamber evacuated to a pressure of $< 10^{-4}$ torr. Once again a few data points were recorded with no target in the beam to check for background effects. In all over 1100 separate runs averaging about 15,000 events each were taken. An "event", as used here, refers to the 38 data words describing TDC and ADC outputs from the wire chambers and scintillators.

Initially at each angle the HRS fields were set to detect protons elastically scattered from ^{1}H; i.e. field settings corresponding to p + p kinematics. At these settings typically 10,000 events from each target were recorded (except LH_2), giving the yield at the quasi-elastic peak. The liquid hydrogen runs consisted of 25 K events, giving the p + p elastic yield. Background runs lasted until the total integrated beam current was that of an average target-in run. Then the HRS fields were decreased to the values for a proton of about 100 Mev/c lower momentum, and the series of targets was run through again. As the momentum of protons at the focal plane was decreased, multiple scattering and energy loss in the scintillators resulted in an increased inefficiency of the HRS trigger. Therefore the definition of the HRS trigger was changed from S1•S2•S3•S4 to S1•S2•S3 at ~ 850 MeV/c, then to S1•S2 at ~ 400 MeV/c. Overlap data were taken at points 100 MeV/c above and below these values to assure consistency. This process was continued until the outgoing proton's kinetic energy was so low as to preclude reliable counting efficiency (50 MeV). A synopsis of the data runs by target, angle and momentum is given in Appendix A.

C. EXPERIMENT 386: TOTAL REACTION CROSS SECTIONS

Experiment 386 was an absolute measurement of the attenuation of an 800 MeV proton beam by nuclei, and as such was greatly different from the usual experiment carried out at the HRS. The extraction of total reaction cross sections from this attenuation will be described

in Chapter III, but here we wish to point out the experimental situation. None of the standard HRS data acquisition system, focal plane detectors, or beam monitors were used. In fact the HRS itself was used only as a focussing lens for 800 MeV protons.

The experimental arrangement is shown in Figure 2.6. Two .010" thick scintillation counters upstream of the target, S1 and S2, counted the beam particles incident on the target. S3 was a scintillator of the same thickness, with a $\frac{1}{8}$" hole drilled in it which served as a veto for the beam halo. A small drift chamber, C1, acted as a beam profile monitor. The construction and operation of this chamber is described in Appendix B. S4 was a veto counter located 27.63" downstream of the target with a 1" hole, defining a solid angle of 1.03 msr. With the HRS set at 0°, S5 and S6 were mounted on the focal plane to intercept 800 MeV protons scattered inside the 1.03 msr veto counter. The two focal plane counters were overlapped as shown, and the HRS fields were set to put the 800 MeV peak just below the overlap region. Thus S5 intercepted transmitted beam particles and the straggling tail down to ~ 3.5 MeV loss.

A certain fraction of the beam was scattered outside the region of acceptance (defined by the 1" hole in S4) by the upstream counters as well as by the target. Consequently target-in runs were compared to target-out runs to determine the scattering by the target alone. But due to the sensitivity of the absolute measurement to systematic effects, the time between target-in and target-out had to be kept to a minimum. For this and other reasons the CAMAC electronics modules were

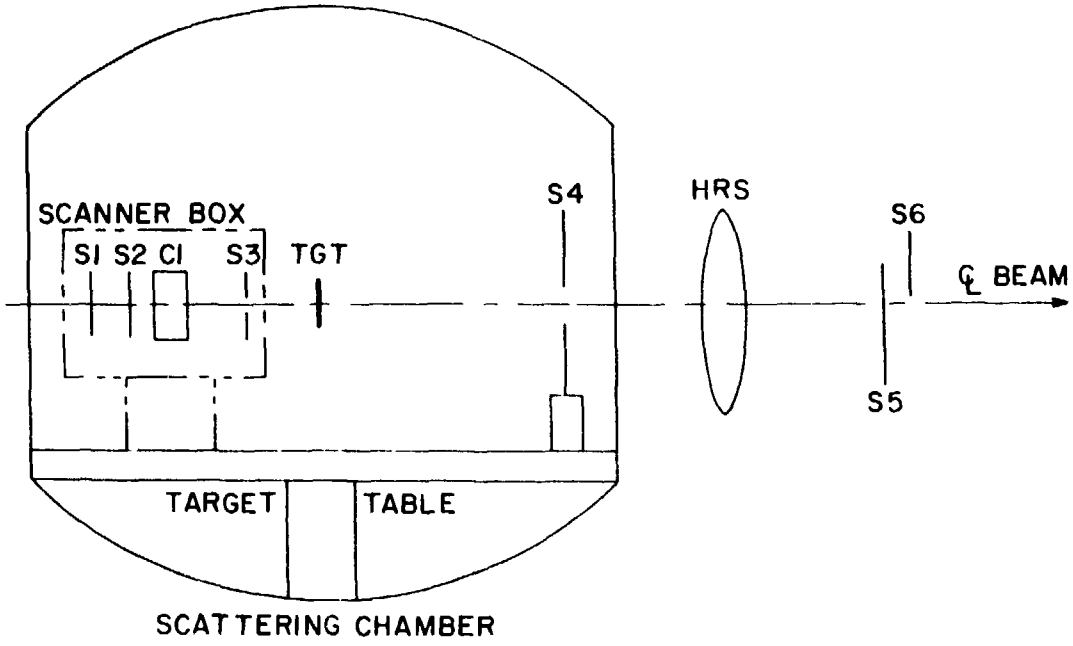

Figure 2.6: Schematic drawing of the experimental arrangement in Experiment 386.

used to change the target configuration every 60 seconds. (Actually the cycle time was chosen at the beginning of each run, but 60 seconds was eventually used as a standard.) A FORTRAN program was written to accumulate various logical combinations of the counter pulses (see below) for a given time, then cease acquisition while the target rotated out of the beam. While the target wheel was moving, accumulated data were written to disk and the CAMAC scalers were cleared. When the target reached its "full out" position, a bit was set in the CAMAC electronics, which had the effect of stopping the target rotation and re-starting the accumulation of data. At the end of the next time period data acquisition again ceased, accumulated data were written as "target-out" data, and the target was rotated back to "full in". So any systematic fluctuations in beam quality or intensity were averaged between target-in and target-out. Further, suspect data could be thrown out without the loss of a large body of it.

Counters S1, S2, S3, and C1 were mounted on a beam scanner which allowed them to be moved independently of the rest of the apparatus. These counters were optically aligned and mounted to a common assembly, which was then attached rigidly to a beam scanner. The scanner had a pair of stepping motors which drove worm gears, providing linear translation of the counter assembly in the two directions perpendicular to the beam. The stepping motors were controlled from inside CCH, and positional readout was supplied there via sliding potentiometers on the scanner. Thus the upstream counter

set could be moved independently and reproducibly up-down and left-right to locate the beam.

In order to accurately extract the total reaction cross section from the attenuation measured in the experiment, it was necessary to know the precise angular span of the S4 veto. As seen in Figure 2.7, for a point beam profile one may assume that all particles scattered outside an angle θ are not counted, and those scattered inside θ are counted. A beam of finite extent, d in Figure 2.7, complicates this assumption: some particles inside $\theta_>$ (but outside θ) are counted, and some particles outside $\theta_<$ (but inside θ) are not counted. Therefore the spatial extent of the beam was critical to the accuracy of the experiment.

The Line C beam optics were tuned to provide a minimally dispersed beam on the target. Once a good tune of Line C was obtained, a phosphor target was put in the scattering chamber and the beam was visually steered onto the crosshairs on the target. Collimator jaws CL04 and CL05 (see Figure 2.1) were used to cut the size of the beam down to less than 1 mm sqare, then an upstream jaw, CL01, was adjusted to cut the beam current down to a countable level. With CL04 and CL05 fixed at a small aperture, drifting in the upstream magnets did not affect the size or location of the beam on the target. The beam profile was then measured by taking a drift time spectrum in C1, and was found to be gaussian in shape with ~ 0.5 mm FWHM. The beam profile was checked periodically with C1.

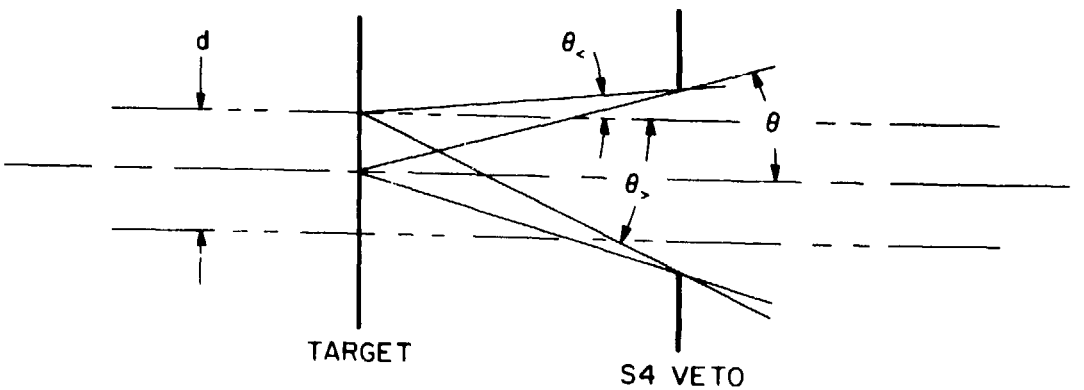

Figure 2.7: For a beam of finite width 'd' the angular span of the veto counter can vary from $\theta_<$ to $\theta_>$.

A similar source of error in the determination of the solid angle can arise if the beam does not travel precisely through the centers of S3 and S4. These counters were centered in the following way: Both S4 and the scanner box containing S1, S2, S3, and C1 were mounted on the target table in the scattering chamber. This table can be rotated from inside CCH, with its angular position relative to some arbitrary reference indicated on a digital readout. With the scanner box lowered below the beam, the target table was rotated left until the beam hit the right edge of the hole in S4. The process was reversed to locate the left edge of the hole. The two values of the table's angular position were averaged and the table was moved to that angle. Line C Steering Magnet 6Y (see Figure 2.1) was used to bend the beam vertically, and the currents through the magnet corresponding to the top and bottom of the hole were recorded. The mean of these values located the beam at the center of S4. With the target table and LC-SM6Y set to their proper values, the scanner box was moved up-down, and right-left to center the hole in S3 about the beam. Thus the line defined by the centers of the two holes was colinear with the beam.

A schematic diagram of the electronics used in the experiment is shown in Figure 2.8. Signals from all scintillators were first discriminated in either Lecroy Research Systems Model 621 or 821 leading edge discriminators. Thresholds were set to - 30 mv and output pulse widths set to 10 ns. Some outputs from these units were further discriminated so their output pulses could be independently widened for use as vetoes in logic units. For example, an output from the S3

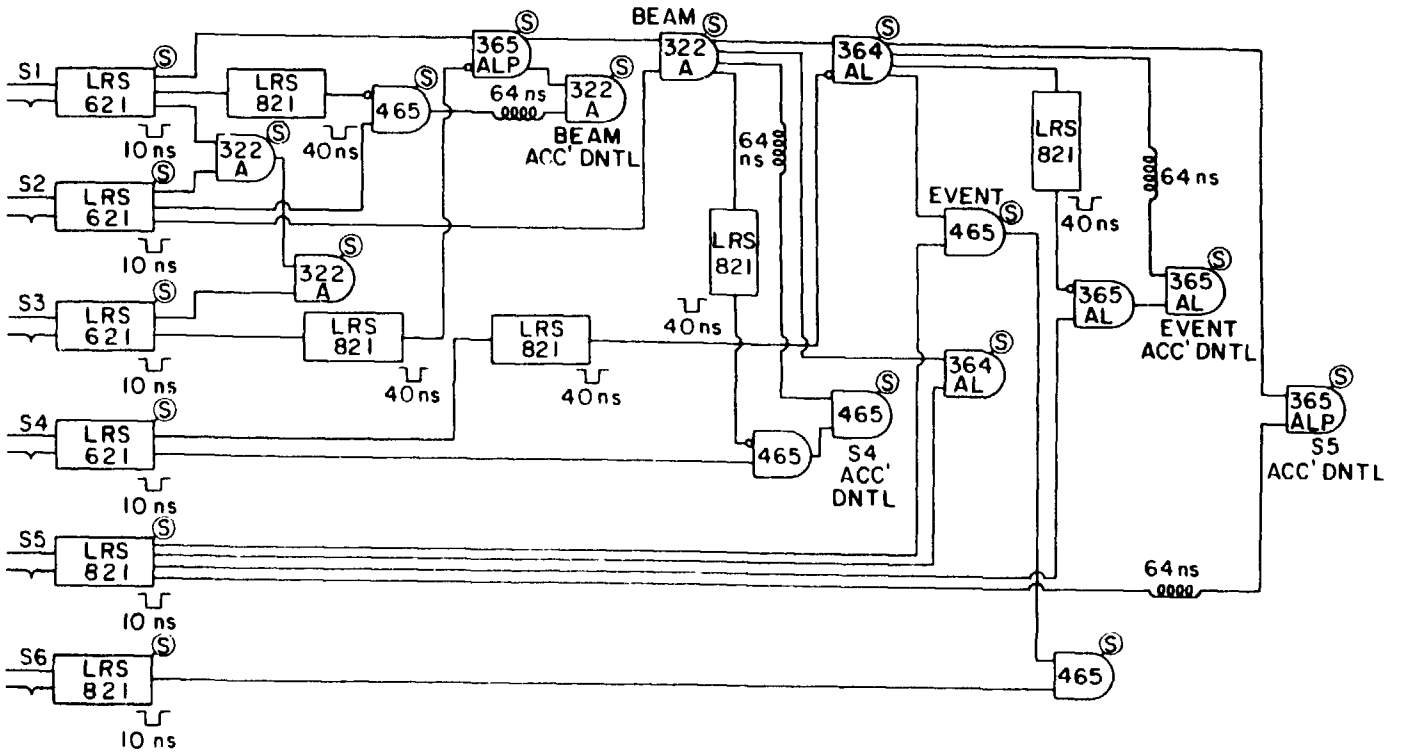

Figure 2.8: Logic diagram of the electronics used in Experiment 386.

discriminator was fed again to a LRS 821 where its output width was set to 40 ns and used as a veto into the LRS 365ALP to give $S1 \cdot \overline{S3}$. An output of this unit was fed to a LRS 322A coincidence register along with the discriminated output of S2 to give $S1 \cdot S2 \cdot \overline{S3}$, or BEAM. The discriminated output of S4 was similarly widened and used as a veto to BEAM in a LRS 364AL. Then $BEAM \cdot \overline{S4}$ was joined with the discriminated S5 signal to form $BEAM \cdot \overline{S4} \cdot S5$, or EVENT. As their names imply, BEAM represented those protons incident on the target, and EVENT represented BEAM particles which scattered inside the 1" hole in S4 and were transmitted through the HRS to S5.

As in any coincidence measurement the possibility exists to count a "true" coincidence (e.g. a beam particle) when in fact an "accidental" coincidence (e.g. two unrelated cosmic rays) has occured. These accidentals are assumed to be uncorrelated in time, so by delaying one of the coincident pair one gets a measure of the probability of accidental overlap of the two signals, i.e.

$$A \cdot B = \text{true}$$

$$A \cdot \text{dld } B = \text{accidental} \quad .$$

However if one knows (or suspects) that most of the singles in either counter come from true coincidences, the above method will overestimate the rate of accidentals. In this case the measure of the number of accidentals should be restricted, specifically how many events are counted as coincidences that are <u>not true</u> coincidences. This may be

accomplished by forming $A \cdot \overline{B}$ and forming a coincidence between this and a delayed signal from B:

$$(A \cdot \overline{B}) \cdot \text{dld B} = \text{accidental} \quad .$$

This was the situation in Experiment 386, so accidentals were dealt with in this way. The discriminated signal from S1 was widened to 40 ns and used as a veto to the discriminated signal of S2 in a LRS 465 logic unit. The output of that unit, $\overline{S1} \cdot S2$, was thus guaranteed not to be a beam particle. This signal was delayed and fed to a LRS 322 coincidence unit with $S1 \cdot \overline{S3}$. The output of that unit was BEAM ACCIDENTALS. Similarly to form EVENT ACCIDENTALS, part of the definition of EVENT, $\text{BEAM} \cdot \overline{S4}$, was widened and used as a veto to the rest of the definition, S5, yielding an S5 event corresponding to no BEAM particle. This signal formed a coincidence with a delayed $\text{BEAM} \cdot \overline{S4}$ signal in a LRS 365AL to give EVENT ACCIDENTALS. Accidental coincidences between S4 and BEAM were formed in a similar manner. This last quantity gave a measure of the accidental vetoing of a good EVENT by S4.

Most of the information described here was scaled, noted (S) on the electronic diagram. The outputs of these various modules were -1.7 v pulses which were connected to 12-channel CAMAC 24-bit scalers. At the end of each "target-in" and "target-out" cycle the accumulated counts in these units was written to disk via the FORTRAN program EXP386, and the scalers were cleared.

CHAPTER III

ANALYSIS OF THE DATA

A. EXPERIMENT 470: REACTIVE CONTENT OF THE OPTICAL POTENTIAL

The off-line analysis of the data from Experiment 470 was done using the standard HRS data acquisition system "Q"[19,20] in a "Must Process" mode. This system consists of three major components: an ANALYZER, a DISPLAY package, and an ALLTEST package. The ANALYZER is primarily responsible for converting the 36 taped words containing time and pulse-height information into physical quantities such as $(x_f, v_f, y_f, \varphi_f)$ and (v_t, φ_t, y_t, v). The ANALYZER also calls a relativistic kinematics subroutine KINREL to correct for the recoil of the target nucleus, arriving at the missing mass. Of course these quantities are complicated functions of times and pulse heights, so in the process of calculating them many other intermediate quantities are also calculated. In all the ANALYZER generates over 200 DATA WORDS which can be displayed or used in the ALLTEST package.

The DISPLAY package, DSP[21], permits the creation of one-dimensional histograms, the entry, retrieval and plotting of these histograms, and the dynamical display of two-dimensional scatter plots as data are acquired. The user can specify which DATA WORD is to be plotted, a test to be passed for entry to the histogram, and display parameters. DSP is therefore closely linked to the ANALYZER and to ALLTEST. In addition one may use cursors on displayed data to define

the limits of GATES and BOXES, which are in turn written as tests to the ALLTEST package.

ALLTEST is a subroutine to the ANALYZER which allows the user to perform tests on raw and calculated DATA WORDS (MICROTESTS) or on logical combinations of previous tests (MACROTESTS). A MICROTEST specifies a bit pattern or upper/lower limits on the value of a DATA WORD (including the limits defined in GATE and BOX commands to displayed data). A MACROTEST specifies logical combinations of previous MICRO- or MACRO-TESTS or their complement (AND, OR, EXCLUSIVE OR). Tests are defined in the Test Descriptor File (see Appendix C) which is written in a clear and concise format to facilitate the evolution of off-line replay of the experiment. Through the Test File one can easily tighten or loosen the definition of a "good" event, define a restricted region of the focal plane, or change Particle Identification limits. The Test File for Experiment 470 was used to count protons scattered into a solid angle $\Delta\Omega$ and momentum interval Δp (Test 76) to arrive at the double-differential cross section. Other tests were used to determine the focal plane efficiency, software efficiency, and normalization of the data.

A.1: The Differential Cross Section

In scattering experiments the number of particles scattered into a solid angle $\Delta\Omega$ is proportional to the beam flux, the size of $\Delta\Omega$, and the number of scatterers intercepting the beam:

$$dN = \sigma(\theta) \cdot N_b \cdot \Delta\omega \cdot n_s \quad . \tag{3.1}$$

The constant of proportionality $\sigma(\theta)$ is the differential cross section and

$$\sigma(\theta) \cdot \Delta\omega = d\sigma(\theta) \tag{3.2}$$

so that

$$\frac{d\sigma(\theta)}{d\omega} = \frac{dN}{N_b \cdot n_s \cdot \Delta\omega} \quad . \tag{3.3}$$

For elastic and inelastic scattering to discrete final states this is the quantity of interest, and beam particles which leave the nucleus in discrete states are easily identified and counted with a spectrometer such as the HRS. However scattering to the continuum does not result in outgoing protons with discrete energy losses. In this region the scattering yield into a solid angle $\Delta\omega$ and momentum interval Δp is

$$dN = \sigma(\theta,p) \cdot N_b \cdot n_s \cdot \Delta\omega \cdot \Delta p \quad , \tag{3.4}$$

and by analogy with Equation 3.2

$$\sigma(\theta,p) \cdot \Delta\omega \cdot \Delta p = d^2\sigma(\theta,p) \tag{3.5}$$

so that the quantity of interest is

$$\frac{d^2\sigma(\theta,p)}{d\Omega\, dp} = \frac{dN}{N_b \cdot n_s \cdot \Delta\Omega \cdot \Delta p} \quad . \tag{3.6}$$

Determination of the right side is the object of the experiment.

A.2: NORMALIZATION

Since the (p,p′) inelastic spectra for excitations greater than about 160 MeV are structureless over the momentum acceptance of the HRS ($\frac{\Delta p}{p} \approx \pm 1.2$ %), and because the angle-integrated (p,p′) cross sections $\frac{d\sigma}{d\Omega}$ are structureless over the solid-angle acceptance of the HRS ($\Delta\theta \approx \pm 1^{o}$ in the plane of scattering), the full phase space acceptance of the HRS was used for each HRS angle-field setting to generate a single data point for the relative $\frac{d^2\sigma}{d\Omega dp}$.

However the momentum-solid angle acceptance function of the spectrometer is not uniform over the entire focal plane, so that a technique had to be devised to obtain the absolute cross sections. This technique, described below, involved using a small region at the center of the focal plane, where the acceptance is uniform, to cross-normalize some of the $\frac{d^2\sigma}{d\Omega dp}$ data to ^{1}H (p,p) elastic scattering data obtained during the course of the experiment. Since the elsastic ^{1}H (p,p) cross sections are known, the absolute cross sections for $\frac{d^2\sigma}{d\Omega dp}$ were easily obtained for the restricted angle-momentum acceptance runs. Then it was simply a matter of scaling the relative $\frac{d^2\sigma}{d\Omega dp}$ data obtained with the full acceptance, to obtain the absolute cross sections.

Figure 3.1, obtained using a CH_2 target with the HRS at 15° and fields set for ^1H (p,p) elastic scattering, shows a scatter plot of events at the focal plane as a function of dispersion coordinate and scattering angle. The diagonal line of events corresponds to protons elastically scattered from the ^1H in the CH_2. The angle-position correlation is due to the large kinematical $\frac{dE}{d\theta}$ (-9.4 MeV/deg) at this angle. Box 7 in the figure was used as a test to constrain the scattering angle to the central 0.3° accepted by the HRS. Because of the large $\frac{dE}{d\theta}$, Box 7 also effectively restricts the focal plane dispersion coordinate to ± 2.1 cm (the focal plane is 60 cm in this direction). The ^1H (p,p) events passing the Box 7 test occur over a central region of the focal plane (~ 0.7 % of the full acceptance) for which the relative momentum-solid angle acceptance is known to be uniform.

For ^1H (p,p) elastic scattering we have

$$\frac{d\sigma(\theta)}{d\Omega} = \frac{K \cdot NB7 \cdot CF}{IC \cdot n_s} \qquad (3.7)$$

where NB7 is the number of counts in Box 7, CF accounts for the efficiencies of the drift chambers relative to the event trigger, IC is a relative current monitor, and n_s is the areal density of scattering centers in the target. Thus the normalization constant K accounts for the gain of the ion chamber, the overall trigger efficiency, and the size of $\Delta\Omega$ defined by Box 7. Since $\frac{d\sigma}{d\Omega}$ for 800 MeV ^1H (p,p) elastic scattering is known[22], K can be calculated.

In order to obtain an absolute normalization for the $\frac{d^2\sigma}{d\Omega dp}$ data, Box 8 (Figure 3.1) was used in the test file to define the same angle limits as Box 7, but a dispersion direction region corresponding to the region indirectly defined by Box 7 for the ^{1}H (p,p) data. Since the trajectory's dispersion coordinate on the center of the focal plane is linear with dispersion

$$x_f = D \cdot \delta = D \cdot \frac{\Delta p}{p} = D \cdot \frac{p_o - p_{sp}}{p_{sp}} \quad , \tag{3.8}$$

where D is the dispersion, p_{sp} is the momentum corresponding to the optic axis for given HRS field settings, and p_o is the momentum of the trajectory. Therefore

$$\Delta p_{Box8} = \frac{p_{sp} \cdot \Delta x_{Box8}}{D} \quad , \tag{3.9}$$

so that

$$\frac{d^2\sigma}{d\Omega dp} = \frac{K \cdot D}{\Delta x_{Box8}} \cdot \frac{NB8 \cdot CF}{IC \cdot n_s \cdot p_{sp}} \quad , \tag{3.10}$$

where NB8 is the number of counts in Box 8. Since K is known from the ^{1}H (p,p) analysis, absolute double-differential cross sections were obtained. However Box 8 selects only a small fraction of the events detected at the focal plane, so the absolute normalization runs were

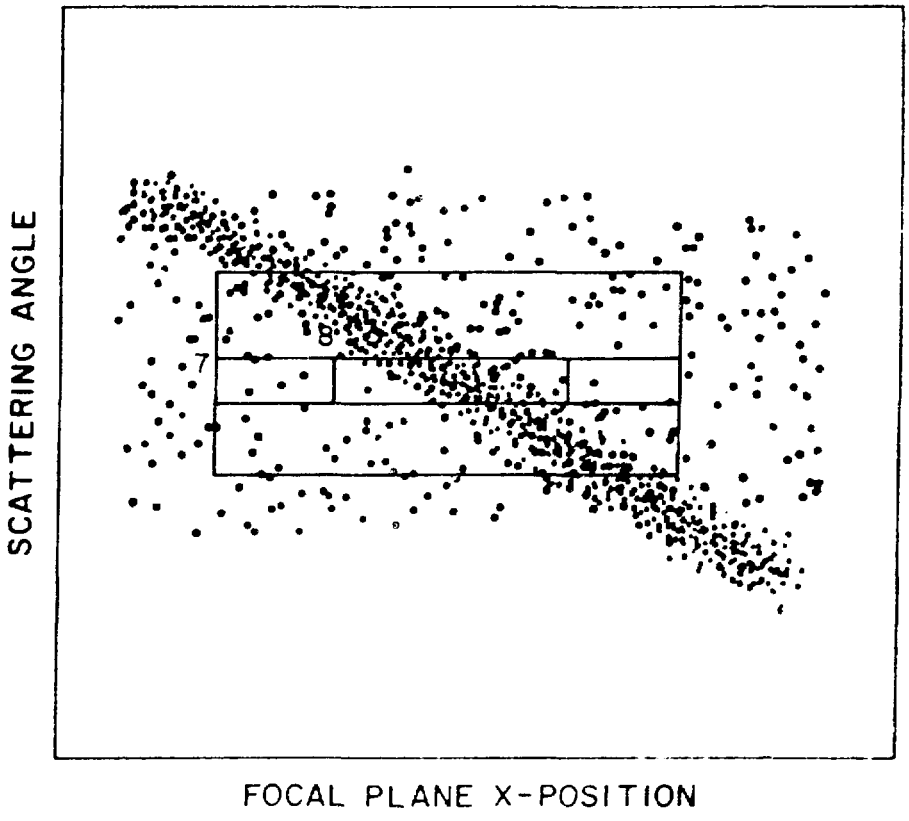

Figure 3.1: Scatter plot of events at the HRS focal plane as a function of position in the dispersion direction ($\hat{x}$) and scattering angle. The diagonal line of events corresponds to elastic scatering from ^{4}H in a CH_2 target.

considerably longer than those runs for which most of the focal plane was used to obtain the relative $\frac{d^2\sigma}{d\omega dp}$.

Box 9, shown in Figure 3.2, was used to obtain the relative double-differential cross sections for all of the runs. As stated earlier, $\frac{d^2\sigma}{d\omega dp}$ is a smooth function of both momentum and angle, and varies little over the momentum- and solid angle-acceptance of the HRS, so that a factor A can be used to cross-normalize the Box 9 derived relative cross sections to the Box 8 derived absolute cross sections obtained from the normalization runs:

$$A \cdot K \cdot \frac{NB9 \cdot CF}{IC \cdot n_s \cdot p_{sp}} \cdot \frac{K \cdot D}{\Delta x_{Box8}} \cdot \frac{NB8 \cdot CF}{IC \cdot n_s \cdot p_{sp}} \quad . \tag{3.11}$$

Thus

$$A = \frac{NB8}{NB9} \cdot \frac{D}{\Delta x_{Box8}} \quad . \tag{3.12}$$

These Box8 - Box9 normalization runs were made in the region 800 MeV/c < p_{sp} < 1000 MeV/c where the cross section is smoothest. The results for several angles and targets were statistically averaged. The final expression to be used in calculating $\frac{d^2\sigma}{d\omega dp}$ is then

$$\frac{d^2\sigma}{d\omega dp} = \frac{A \cdot K \cdot NB8 \cdot CF}{IC \cdot n_s \cdot p_{sp}} \quad . \tag{3.13}$$

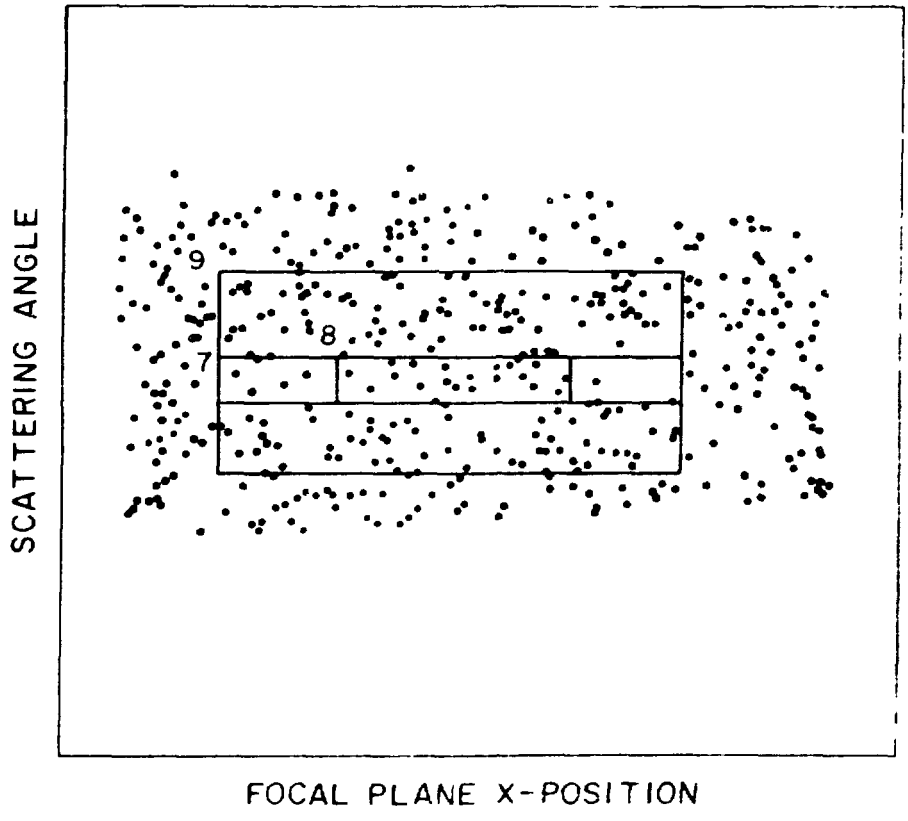

Figure 3.2: See Figure 3.1. These data were taken at energy-loss corresponding to pion production. Boxes 7, 8, and 9 are discussed in the text.

The HRS acceptance is a function of beam-on-target width in the non-dispersion direction. For thin targets the region of uniform acceptance is about $\pm \frac{1}{2}$ cm in the direction transverse to the optic axis of the HRS. Since the beam-on-target width is typically less than $\pm \frac{1}{4}$ cm, no problems are encountered.

However for the 5 cm cylindrical LH_2 target used during Cycle 25, the beam-target volume was 5 cm long in the beam direction, so that the "effective" target thickness seen by the HRS (Figure 3.3) varied with spectrometer angle. Therefore during the LH_2 runs $^1H(p,p)$ elastic were also taken at each angle using a solid CH_2 target, and the normalization of this solid-target data made it possible to account for the variation in the effective target thickness of the liquid-target data. The CH_2 data were normalized using the Box 7 technique described above.

Finally it is to be noted that the IC gain was different for the two running cycles. Since normalization data using the CH_2 target were obtained for both Cycles 25 and 26, the different ion chamber gains presented no problem. As a further check of the normalization elastic scattering data were taken for $p + {}^{208}Pb$ at $\theta_{lab} = 5^\circ$ during Cycle 26, and compared to the data of Hoffmann et al[23]. The two normalizations thus got agreed to within 2 %.

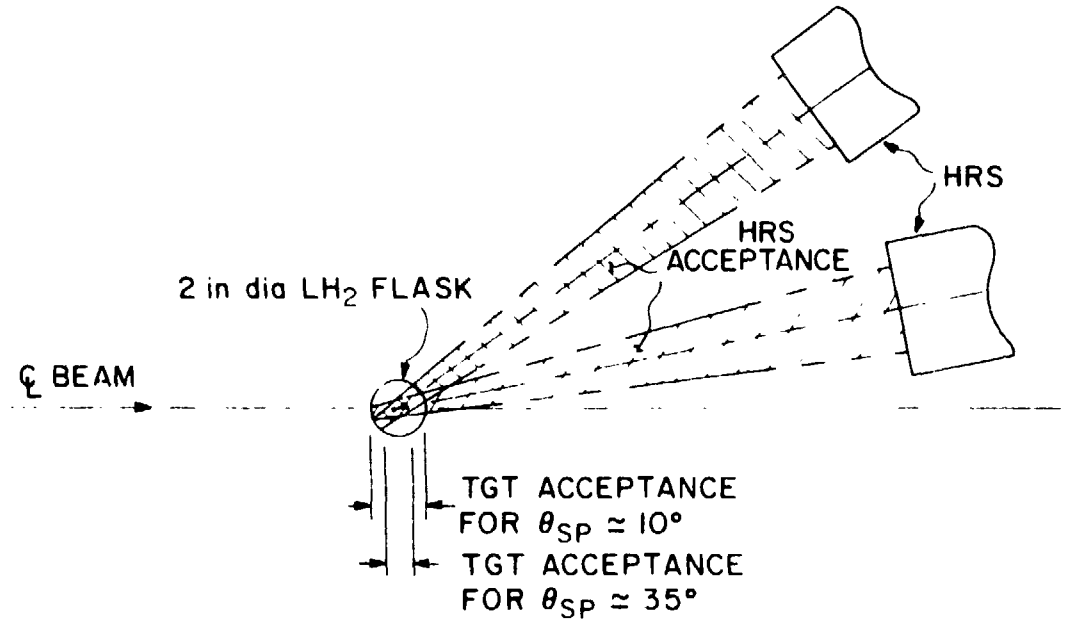

Figure 3.3: The HRS acceptance region (shaded area) has a width at the target of $\sim \frac{1}{2}$cm. This produces an effective target thickness which changes with angle.

A.3 BACKGROUNDS

The scheme outlined above assumes that the scattering is from a pure target. In fact, however, protons scattered from impurities in the targets, Helium in the scattering chamber, and the LH_2 target flask were also detected. It was necessary to subtract such events from the data in order to arrive at meaningful results. Further, extraction of $^1H(p,p')$ inelastic information from data obtained using the CH_2 target required that scattering from ^{12}C be accounted for.

For all targets, including LH_2, target-in and target-out measurements were made to determine the background contribution. For the LH_2 runs the background due to the Mylar flask was typically 5 %. For the solid-target data obtained during Cycle 25, the Helium in the scattering chamber contributed between 3 % and 20 % to the total yield. Background during Cycle 26 were typically 5 %.

Extraction of the $^1H(p,p')$ cross sections from CH_2 cross sections was a similar exercise:

$$\left(\frac{NBS \cdot CF}{IC \cdot n_{CH_2}}\right)^* = \left(\frac{NBS \cdot CF}{IC \cdot n_{^1H}}\right)^* + \left(\frac{NBS \cdot CF}{IC \cdot n_{^{12}C}}\right)^* \qquad (3.14)$$

where the * indicates that backgrounds have been subtracted. Then

$$\left(\frac{d^2\sigma}{d\Omega\, dp}\right)_{^1H} = \left(\frac{d^2\sigma}{d\Omega\, dp}\right)_{CH_2} - \frac{1}{2}\left(\frac{d^2\sigma}{d\Omega\, dp}\right)_{^{12}C} . \qquad (3.15)$$

One more adjustment to the ^{40}Ca data was made. Figure 3.4 is a spectrum of protons elastically scattered from the ^{40}Ca target at 5°. The second peak seen corresponds to protons elastically scattered from a lighter nucleus, in this case an ^{16}O contaminant. Since data were not taken on ^{16}O, no definitive number was available to be subtracted, so the assumption was made that

$$\left(\frac{d^2\sigma}{d\Omega\, dp}\right)_A \propto A^{0.67} \qquad (3.16)$$

based on total reaction cross section measurements. Then

$$\left(\frac{d^2\sigma}{d\Omega\, dp}\right)_{^{16}O} = 1.21 \left(\frac{d^2\sigma}{d\Omega\, dp}\right)_{^{12}C} , \qquad (3.17)$$

and the ^{40}Ca data were adjusted accordingly.

A.4: Uncertainties

Aside from statistical uncertainties in the data and backgrounds, there are three sources of uncertainties in the results: target thickness, the derivation of A in Equation 3.12, and overall normalization of the data.

The target thicknesses were known to 2 %, and this error is included as an uncertainty in n_s.

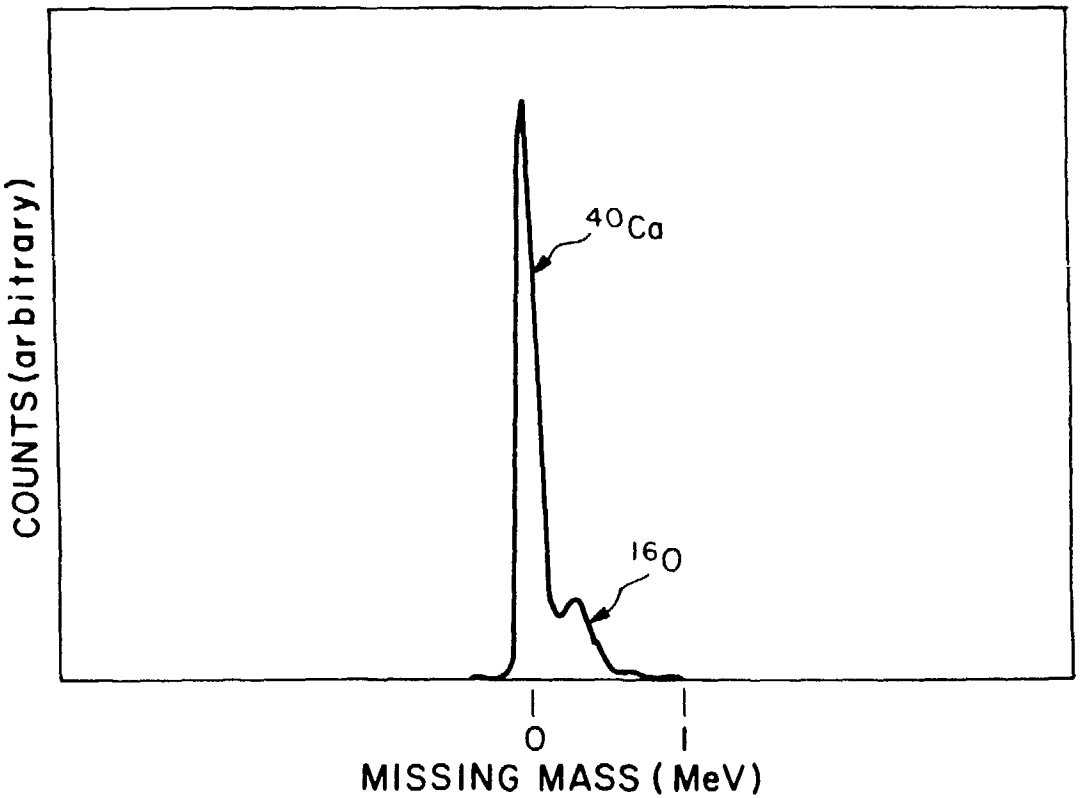

Figure 3.4: Histogram of Missing Mass for p + ^{40}Ca elastic scattering at $\theta_{lab} = 5^{\circ}$. The ^{16}O contaminant is displaced by the kinematical difference between scattering from an A=40 target and an A=16 target.

The error in the determination of A by Equation 3.12 is

$$\frac{\Delta A}{A} = \left[\left(\frac{\Delta NB8}{NB8}\right)^2 + \left(\frac{\Delta NB9}{NB9}\right)^2\right]^{\frac{1}{2}} \quad . \tag{3.18}$$

By calculating A for different angles and targets, several values (with errors) were obtained and statistically averaged. The distribution of A's had a χ^2 of 0.7, so calculation of the errors by purely statistical means may have overestimated them slightly. These quantities were nonetheless used in the reported results.

The assumption that generates Equation 3.8, namely that δ is linear in $\hat{x}_f$, does have some inherent error, but these higher order terms in δ are ~ 0.4 % and so were ignored.

Apart from the above uncertainties, the uncertainty in the overall normalization of the data depends on the uncertainty associated with the data used to determine the absolute normalization. Both the 800 MeV p + p and p + ^{208}Pb elastic data used for this normalization have quoted uncertainties of 5 %.

A.5: RESULTS

The results of the experiment are shown in Figures 3.5-3.9, and in Appendix A. Also shown in the figures are the (renormalized) data of Chrien, et al[24] for the quasi-elastic region. The data obtained in this experiment and the Chrien data have absolute normalizations which differ by from 11 % to 25 %, depending on target and angle.

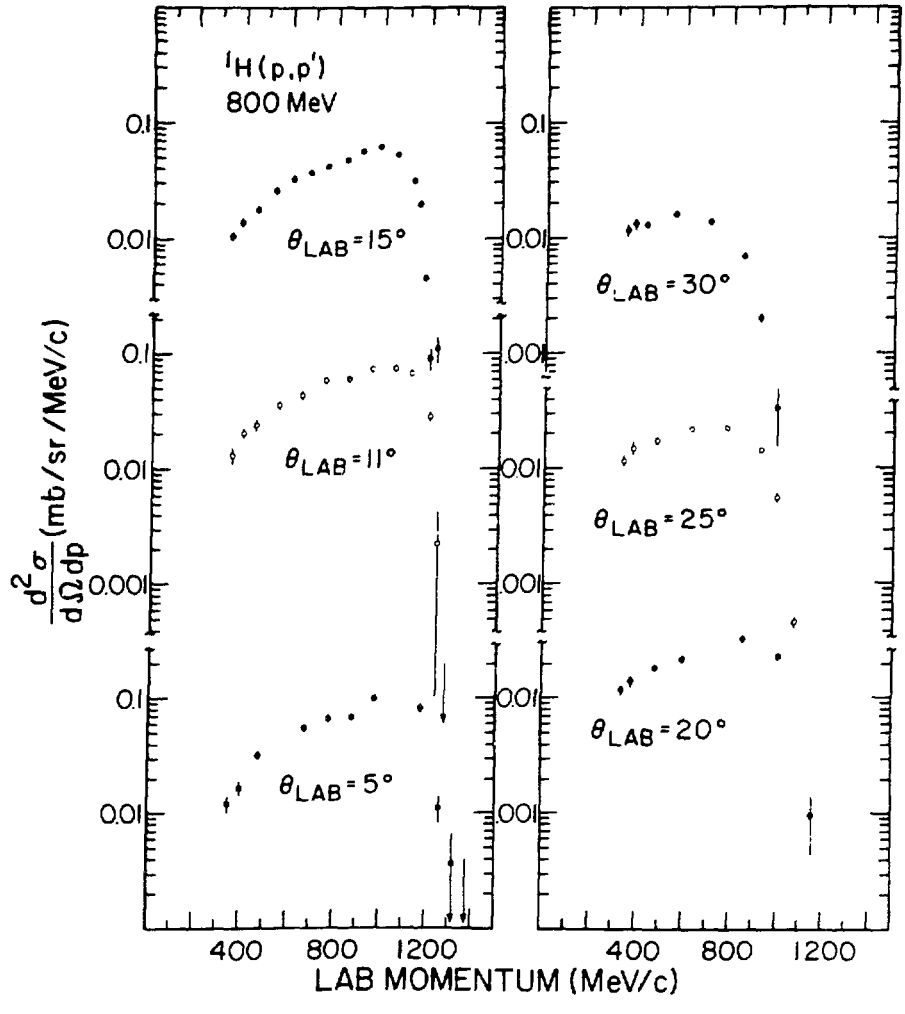

Figure 3.5: The double-differential inclusive cross section for ^{1}H(p,p') scattering at 800 MeV.

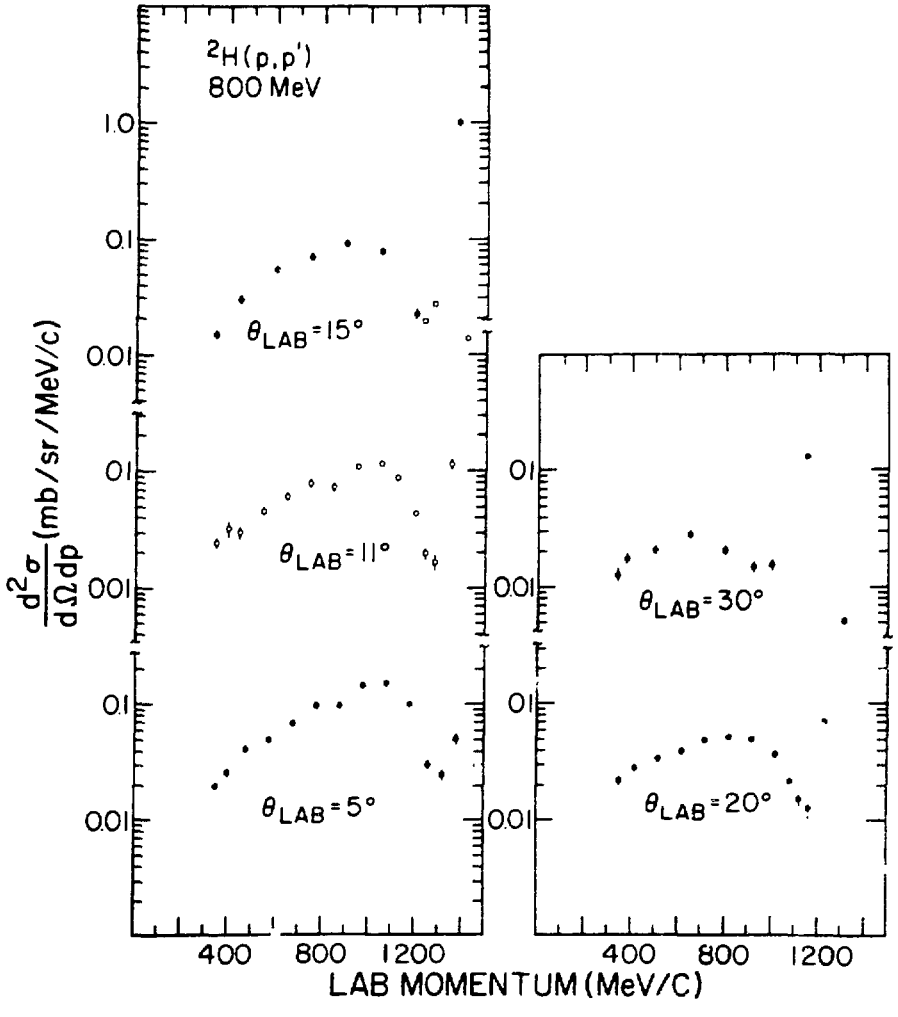

Figure 3.6: Same as Figure 3.5, for ^{4}H(p,p').

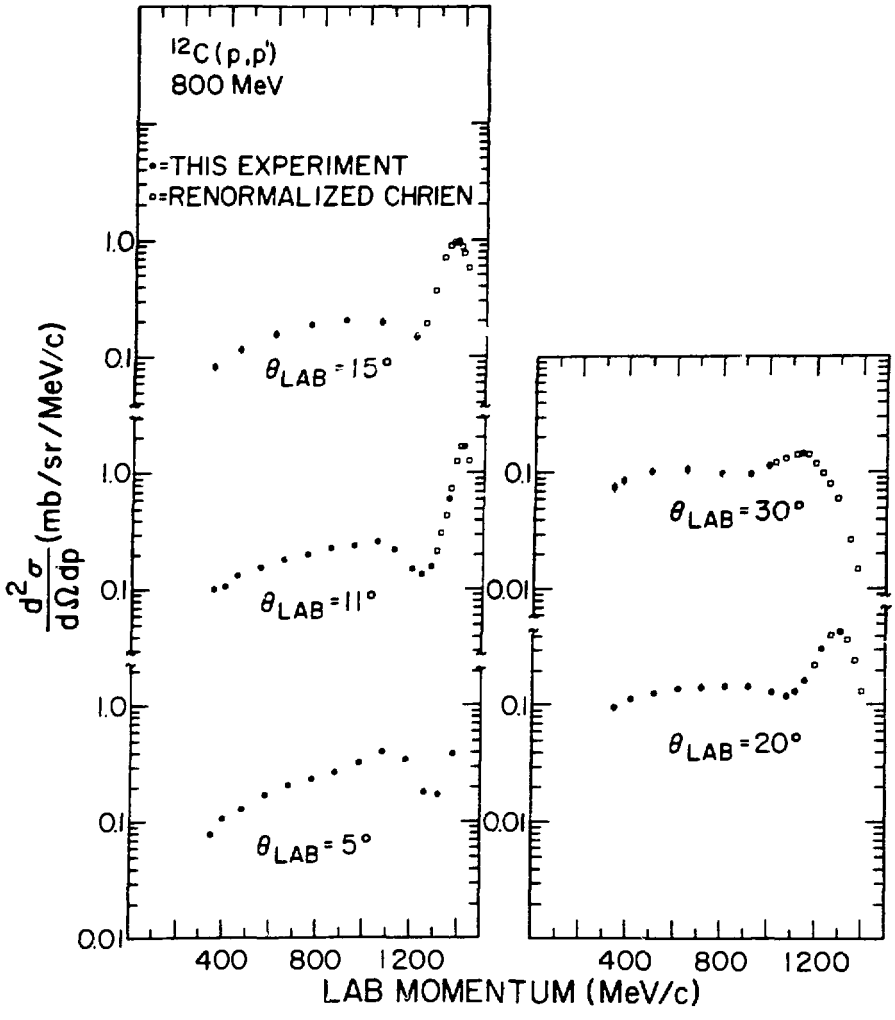

Figure 3.7: Same as Figure 3.5, for $^{12}C(p,p')$.

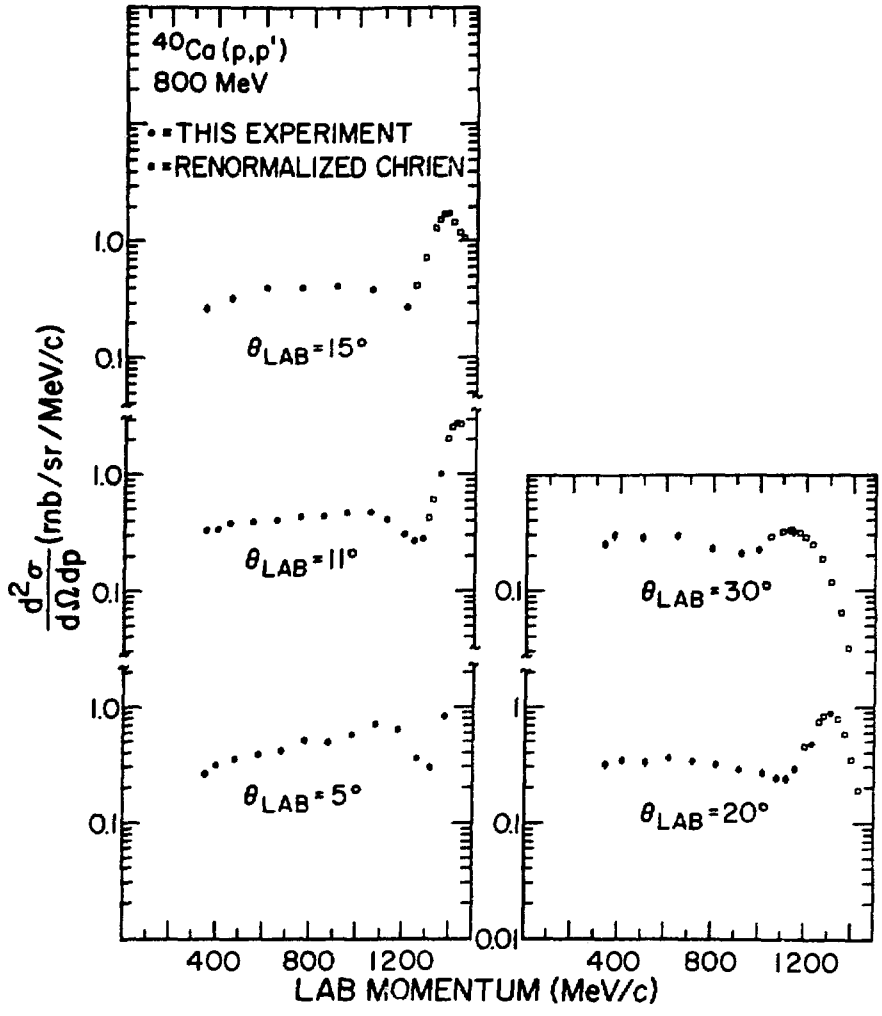

Figure 3.8: Same as Figure 3.5, for $^{40}Ca(p,p')$.

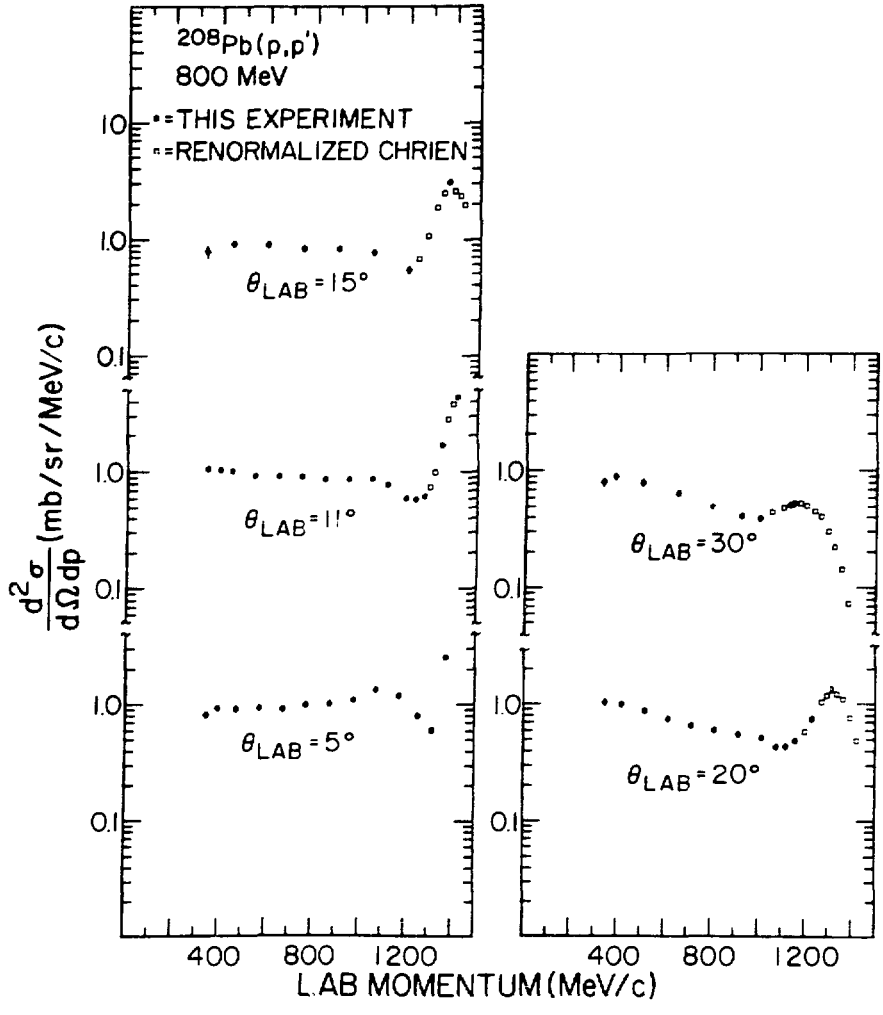

Figure 3.9: Same as Figure 3.5, for ^{208}Pb(p,p').

B: EXPERIMENT 386: TOTAL REACTION CROSS SECTIONS

B.1: The Attenuation Cross Section

In the off-line analysis of the Experiment 386 data the attenuation cross section was calculated from the recorded data, and reaction cross sections were calculated from the attenuation cross sections. The attenuation of a particle beam by a target of density ρ is described by

$$N = N_o \cdot e^{-\rho\sigma x} \quad , \tag{3.19}$$

where N_o is the number of beam particles, N is the number of particles transmitted through the target, x is the target thickness, and σ is the attenuation cross section. This experiment was performed with counters upstream of the target, and they scattered ~ 0.3% of the beam. In fact those counters scattered a fraction of the beam that was on the order of the fraction scattered by the targets. Denoting i_o and i as the beam and transmitted particles, respectively, with no target in the beam; and I_o and I as those quantities with the target in the beam

$$i = i_o e^{-\rho_c \sigma_c x_c} \quad , \tag{3.20}$$

$$I = I_o e^{-(\rho_c \sigma_c x_c + \rho_A \sigma_A x_A)} \quad , \tag{3.21}$$

where the subscript A refers to the target nucleus, and c to the counters. Then the attenuation cross section due only to the target is

than 0.1 mb, or a contribution to the reaction cross section of around one part in 10^4.

B.3b Straggling: The straggling of the beam in both the upstream counters and in the target can cause a fraction of the transmitted beam to miss the EVENT detector S5; i.e. those particles degraded by more than ~ 3.5 MeV will be bent by the HRS away from S5. Of course, straggling will not affect the counted BEAM, I_o and i_o, so denoting the measured quantities with primes,

$$I = I' + I_{strgl} \tag{3.24}$$

$$i = i' + i_{strgl} \tag{3.25}$$

where I_{strgl} (i_{strgl}) is the portion of the transmitted beam not counted due to straggling in S1, S2, and the target (S1 and S2 only). Since $\rho\sigma x$ is small (<.01), Equation (3.22) can be written

$$\sigma_A = \frac{S}{\rho x} \tag{3.26}$$

where

$$S = \left(\frac{i}{i_o} - \frac{I}{I_o}\right) \tag{3.27}$$

Then

$$\sigma_A \sim \frac{1}{\rho x}\left(S' + \frac{i_{strgl}}{i_o} - \frac{I_{strgl}}{I_o}\right) \quad . \tag{3.28}$$

With no target in the beam the fraction lost, c_s, is due only to to the scintillators S1 and S2

$$i_{strgl} = c_s i_o \quad , \tag{3.29}$$

and with the target in the beam the fraction lost is due to both the scintillators S1 and S2 (c_s) and to the target (c_t)

$$I_{strgl} = (c_s + c_t) I_o \quad . \tag{3.30}$$

So Equation 3.28 becomes

$$\sigma_A = \frac{1}{\rho x}(S' - c_t) \tag{3.31}$$

and the fractional error in σ_A due to straggling loss is

$$\frac{\Delta\sigma_A}{\sigma_A} = \frac{c_t}{S} \quad . \tag{3.32}$$

Calculations of the straggling tail to energy losses greater than about 3.5 MeV were made using the program LANDAU, based on the theory of Vavilov[28]. An uncertainty of 35 mb was calculated for the ^{208}Pb target. For the other targets $\frac{c_t}{S} < .01$.

$$\sigma_A = -\frac{1}{\rho_A x_A} \ln \left(\frac{I\, i_o}{I_o\, i}\right) \qquad (3.22)$$

Accidentals, as discussed in Chapter II, were subtracted from I_o, I, i_o, and i before calculating S.

B.2: Reaction Cross Section

The transmitted particles in I consisted of unscattered beam particles, and particles scattered both elastically and inelastically inside the solid angle ω defined by the downstream veto counter S4. There are few inelastic events at 0°, and most of those were bent by the HRS away from the EVENT counter S5. Therefore

$$\sigma_A = \sigma_R + \int_{>\omega} d\omega' \frac{d\sigma_{el}}{d\omega'} \quad . \qquad (3.23)$$

The problem of accurately extracting reaction cross sections from attenuation cross sections, then, is that of knowing the elastic cross sections outside ω, and of knowing ω.

For the nuclei discussed here the elastic cross sections have been measured[13,25,23] to an accuracy of 5 % in the angular range $2° < \theta_{lab} < 22°$, at which point they have dropped by a factor of ~ 10^6. The contribution to the integral for angles outside 22° was therefore negligible.

The veto counter S4 defined an azimuthal angle of $\sim 1^{\circ}$, so there remained a small region inside 2° for which the elastic cross section had to be calculated. The Optical Model fitting routine RELOMN[26] was used to calculate that cross section for $1^{\circ} < \theta_{lab} < 2^{\circ}$. The calculated cross sections were constrained to fit the data for $2^{\circ} < \theta < 10^{\circ}$, and since the $\theta < 2^{\circ}$ region is dominated by Coulomb scattering, the calculated values were considered more than sufficient.

B.3: Systematic Errors and Corrections

One must consider three possible corrections to the extraction of reaction cross sections as oulined in the scheme above: inelastics transmitted to the EVENT counter S5, straggling, and Multiple Coulomb Scattering. The contribution made by these processes to the reaction cross section will be discussed here. Further, possible sources of error associated with the uncertainty in the measurement of θ, uncertainties in the known elastic cross sections, and statistical uncertainties will also be discussed.

B.3a Forward Inelastics: The correction due to forward-scattered inelastic events was negligible. One has to consider only protons scattered at angles less than 1° to states of Ex < 3.5 MeV in the target nucleus: in ^{40}Ca the $(0^{+},3.35)$; and in ^{208}Pb the $(3^{-},2.61)$ and $(5^{-},3.20)$. Data for these reactions are available[13,27] only for angles greater than $\sim 4^{\circ}$, so estimating their contribution for the range $0^{\circ} < \theta < 1^{\circ}$ by the cross section at 4°, one obtains values less

B.3c Multiple Coulomb Scattering: Coulomb scattering is part of the elastic cross section and is accommodated in Equation 3.24. Multiple Coulomb scattering, on the other hand, is a stochastic process which involves repeated small angle scattering, and is equivalent to a diffusion in the plane of θ. Single scattering events to angles outside Ω are properly included in the elastic cross section, but multiple scattering events to those angles are not. The angular distribution of multiply scattered events, based on the expansions presented by Bethe[29] and Scott[30], was determined using the program MOLIER. Multiple Coulomb scattering to angles greater than $\sim 1^{\circ}$ contributed about 50 mb to the measured attenuation for ^{206}Pb, or about 3 % of the reaction cross section. Assuming the correction is accurate to 10 %, an additional 0.3 % uncertainty is added to the uncertainty in the lead cross section. For the other nuclei reported, both the correction and the uncertainty are negligible. The MOLIER results are presented in Table 3.1.

B.3d Uncertainties: Uncertainties in the determination of Ω give rise to an uncertainty in the amount of elastic cross section to subtract from the attenuation cross section. First, there is the question of the size of the veto counter S4. The diameter of this hole was measured to an accuracy of ~ .010", resulting in an angular uncertainty of 0.01°. The contribution of this error to the reaction cross section depends on the shape of the elastic cross section in the vicinity of 1°. For the worst case, that of ^{206}Pb, the elastic cross section is about 2.3×10^{6} mb/sr, so an uncertainty of 0.01° results in an error of

± 30 mb. A second source of error due to x is the position of the beam relative to the center of the hole in S4. The process of locating the center of that hole was carried out twice, about 40 hours apart, and the results were repeated exactly. Since the position was read to ± 0.01°, it seems safe to assume that this location was known to ±0.03°; such an error contributes less than 10 mb to the integral of the elastic cross section for ^{208}Pb, less for the other nuclei.

Target thicknesses were assumed accurate to 2 %.

Another source of error in the extraction of the reaction cross sections is the error in the known elastic cross sections[13,25,23]. Error bars on these data are ~ 5%, and contribute to the reaction cross sections differently for different nuclei. For example, there is an uncertainty in the ^{12}C reaction cross section of ~ 5 mb due to the 5% error in the elastic, whereas the 5% translates to ~130 mb in ^{208}Pb.

From the expression 3.22 for σ_A statistical uncertainties are

$$\delta\sigma_A = \frac{1}{\rho x} \frac{I_o i}{I\, i_o} \cdot \sigma \left(\frac{I\, i_o}{I_o i}\right) \quad . \tag{3.33}$$

The statistical uncertainty of the quantity in parentheses results entirely from δI and δi, since I_o and i_o measure the beam, whereas I and i represent, to some accuracy, the effect of a probabilistic process on the beam. Then

$$\delta\sigma_A = \frac{1}{\rho x} \left[\left(\frac{\delta I}{I}\right)^2 + \left(\frac{\delta i}{i}\right)^2\right]^{\frac{1}{2}} \quad . \tag{3.34}$$

Finally with

$$\delta I = \left[I \left(1 - \frac{I}{I_o}\right) \right]^{\frac{1}{2}} \tag{3.35}$$

$$\delta i = \left[i \left(1 - \frac{i}{i_o}\right) \right]^{\frac{1}{2}} \tag{3.36}$$

one has

$$\delta\sigma_A = \frac{1}{\rho x}\left(\frac{1}{I} - \frac{1}{I_o} + \frac{1}{i} - \frac{1}{i_o}\right)^{\frac{1}{2}} . \tag{3.37}$$

From this final expression it can be seen that the scattering by the upstream detectors contributes to the uncertainty on an equal footing with the scattering by the target, indicating the advisibility of using the thinnest possible BEAM counters. (Note the expressions (3.35) and (3.36) seem somewhat different from those commonly used in scattering experiments. The apparent difference arises from an approximation normally employed to reduce a Binomial distribution to a Poisson distribution[31], so that $\Delta N = \sqrt{N}$. The assumption in the approximation is that the probability deduced is small. Such is not the case in a transmission experiment, since $\frac{I}{I_o} \sim 1$.)

B.4: RESULTS

The extracted total reaction cross sections and various contributions to their errors are presented in Table 3.1.

	Contributions (mb)			Uncertainties (mb)						
Target	σ_A	$\int_{>\Omega} \frac{d\sigma_{el}}{d\Omega'}$	HCS	Stat	$\frac{d\sigma_{el}}{d\Omega}$	n_s	HCS	Stragl	$\Delta\Omega$	$\sigma_R \pm \Delta\sigma_R$
^{12}C	376	98	---	2.5	4.9	7.5	---	---	--	278 ± 9.3
^{40}Ca	1126	406	---	10.2	20.2	22.5	---	---	--	622 ± 32 *
^{208}Pb	4455	2569	50	136.	128.	89.	5	35	32	1836 ± 212

* Includes a correction of 98 ± 4 mb due to ^{16}O contaminant.

TABLE 3.1: Contributions and uncertainties in the calculation of total reaction cross sections (σ_R) as discussed in the text.

CHAPTER IV

SUMMARY AND CONCLUSIONS

The experiments described in the preceding chapters were carried out to provide data which test the main assumption used in practical applications of multiple scattering theory: use of the impulse approximation. The effect of this approximation is to restrict the allowed reaction channels to those initiated by nucleon-nucleon collisions: nucleon knockout and quasi-free pion production. In order to provide a basis for comparison with p + nucleus data, a complete set of p + p inclusive cross sections was obtained. A discussion of the ^{1}H(p,p′) data is given in Section A. Section B presents the p + nucleus data, and Section C discusses the conclusions that can be drawn from the data.

A: THE HYDROGEN SPECTRUM

Figure 3.5 shows the inelastic ^{1}H (p,p′) spectrum at lab angles up to 30°. This spectrum corresponds almost entirely to single pion production. At 800 MeV the process of single pion production proceeds primarily through the p-wave resonance Δ_{33} ($J = \frac{3}{2}$, $T = \frac{3}{2}$), and has been explained most successfully in terms of One Pion Exchange (OPE)[33,34]. Therefore the diagrams assumed to contribute to the ^{1}H (p,p′) inelastic spectrum are those shown in Figure 4.1.

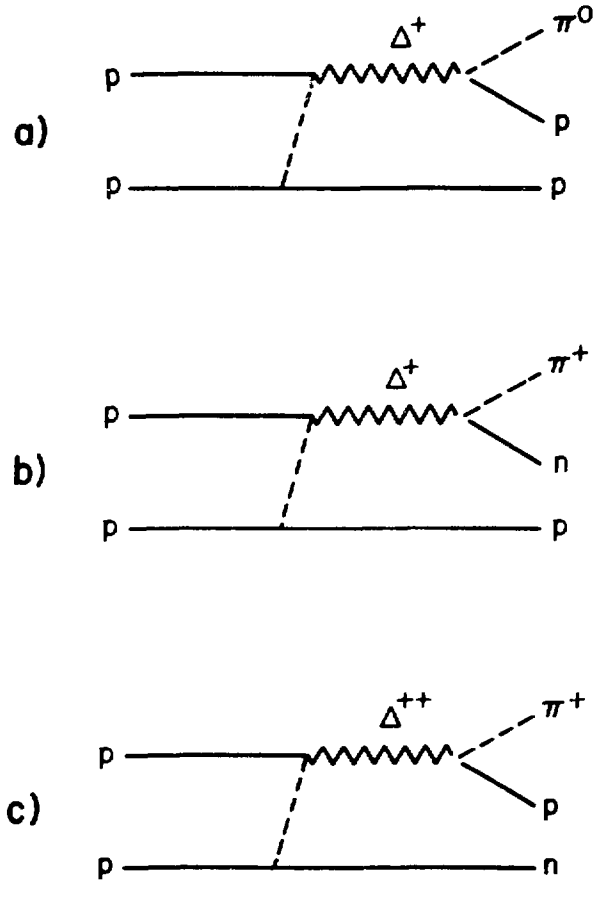

Figure 4.1: The One-Pion-Exchange diagrams for p + p scattering.

The shape of the inelastic $^1H(p,p')$ spectra can be understood as two peaks superposed on one another: a broad peak extending from pion production threshold (Ex ≅ 140 MeV) down to $p_{out} = 0$, which corresponds to the spectrum of protons from the decay of the Δ_{33} resonance (diagrams (a) and (c), Figure 4.1); and a second, narrower peak which represents protons recoiling from the Δ_{33} (diagrams (a) and (b), Figure 4.1). These protons have a quasi-two-body kinematical relation to p_{out}, and show up in the inelastic spectrum as a Breit-Wigner shape centered at Ex ≅ 300 MeV and FWHM ≅ 100 MeV.

Finally, the experimental yield can be estimated by assuming that the cross section for NN → NΔ is given by σ_Δ. Calculating the Clebsch-Gordan coefficients for the addition of isospin gives $\sigma_a = \frac{1}{6}\sigma_\Delta$, $\sigma_b = \frac{1}{12}\sigma_\Delta$, and $\sigma_c = \frac{3}{4}\sigma_\Delta$, where σ_a, σ_b, and σ_c are the cross sections for diagrams (a), (b), and (c) in Figure 4.1. Thus reaction (c) is counted in the broad Δ break-up peak, reaction (b) shows up in the quasi-two-body Breit-Wigner peak, and reaction (a), a two-proton final state, is counted twice. Therefore integration of the spectra in Figure 3.5 over angle and momentum will overcount the total inelastic cross section by the amount contributed by diagram (a), or $\frac{1}{6}\sigma_\Delta$. Such an integration yields 23 ±2 mb, which is expected to be $\frac{7}{6}\sigma_\Delta$, so that σ_Δ is 19.7 ±2 mb.

The cross section for $^1H(p,p)$ elastic scattering measured during this experiment is shown as open circles in Figure 4.2. The data were normalized to the small angle data of Wriekat. Integration

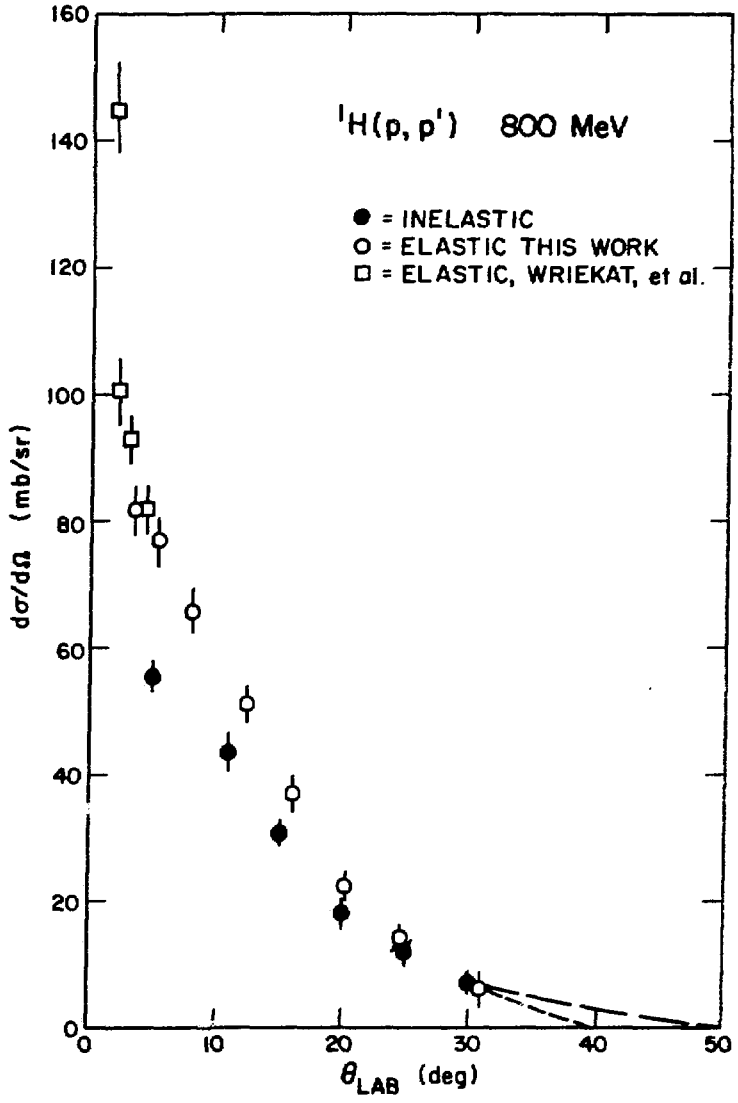

Figure 4.2 : Angular distributions of the elastic cross section (open circles) and the momentum-integrated inelastic cross section (solid dots) for 800 MeV ^{1}H(p,p') scattering.

of the elastic data yields σ_{el} = 25.1 ± 1.2 mb. From this interpretation one concludes that $\sigma_T(p+p) = \sigma_{el} + \sigma_\Delta$ = 44.8 ± 2.3 mb.

The experimental yield from a p + n experiment can be similarly evaluated by assuming the contributing diagrams in Figure 4.3. The scattered proton in diagram (a) has a quasi-two-body kinematical relationship, that in diagram (c) will be counted in the broad break-up region, and diagram (b) will be counted twice. Diagram (d) has no proton in the outgoing channel, so the contribution it makes to σ_Δ will be lost; however its Clebsch-Gordan coefficient is equal to that for diagram (b) (which is over-counted), so the integration over angle and momentum will yield the correct value of σ_Δ.

B: NUCLEAR INELASTIC SPECTRA

The inelastic spectra for p + nucleus scattering are shown in Figures 3.6-3.9.. The outstanding feature of the spectral distributions is their marked similarity to the p + p spectrum, indicating that nucleon-nucleon processes dominate highly inelastic p + nucleus scattering. At the large momentum end of each spectrum is a peak corresponding to quasi-elastic nucleon-nucleon scattering. This region has been investigated at an incident proton energy of 800 MeV by Chrien et al.[24], and their data are shown in the figures as open squares. There is some discrepancy between Chrien's normalization and ours, as discussed in Chapter III. The points shown conform to the normalization of this experiment.

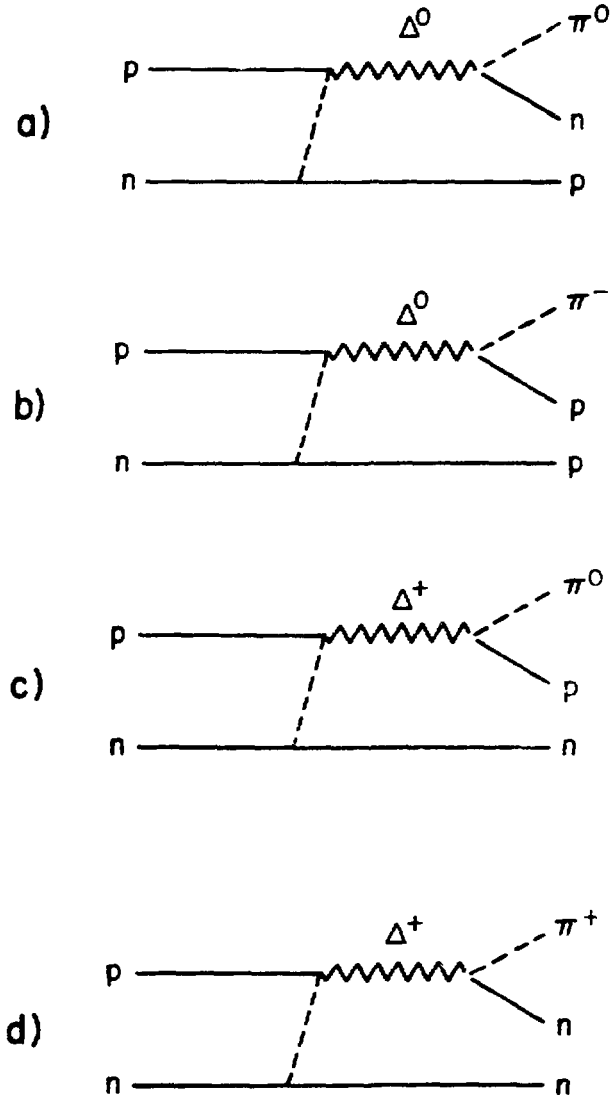

Figure 4.3 : The One-Pion-Exchange diagrams for p + n scattering.

At outgoing momenta lower than that of the deep minimum in the spectra, the same structure can be seen for p + nucleus scattering as for p + p scattering. Because of this similarity of shape and position, these lower momentum data are assumed to be the result of quasi-free Δ-production. The similarity between the p + p inelastic spectrum and the p + nucleus highly inelastic spectra deteriorates for heavier nuclei: whereas the p + ^{2}H data are essentially identical to the p + p data (except for a scale factor), the p + ^{208}Pb data resemble the p + p data only at small scattering angles. Indeed, for ^{208}Pb at $\theta_{lab} = 30^{o}$ the cross section in the quasi-free Δ region increases monotonically with decreasing p_{out}. Such behavior with increasing A and θ_{lab} is to be expected, since the effect of the nuclear medium on the outgoing proton grows with nuclear size (A) and with lower outgoing momentum in the (A+1) - body center of mass.

Further evidence of the dominance of nucleon-nucleon processes in the highly inelastic nucleon-nucleus spectra is the kinematical relation of the prominent peaks seen, namely the quasi-elastic peak and Breit-Wigner peak corresponding to a proton recoiling from a [illegible]. Figure 4.4 shows the momentum corresponding to the center of these peaks as a function of θ_{lab} for ^{12}C. While the distortion effects referred to above inhibit an accurate determination of the peak locations at the larger angles, comparison of the rough locations of these prominences with the curves corresponding to p + p kinematics and p + ^{12}C kinematics leads to the conclusion that the dominant processes observed are between two nucleons.

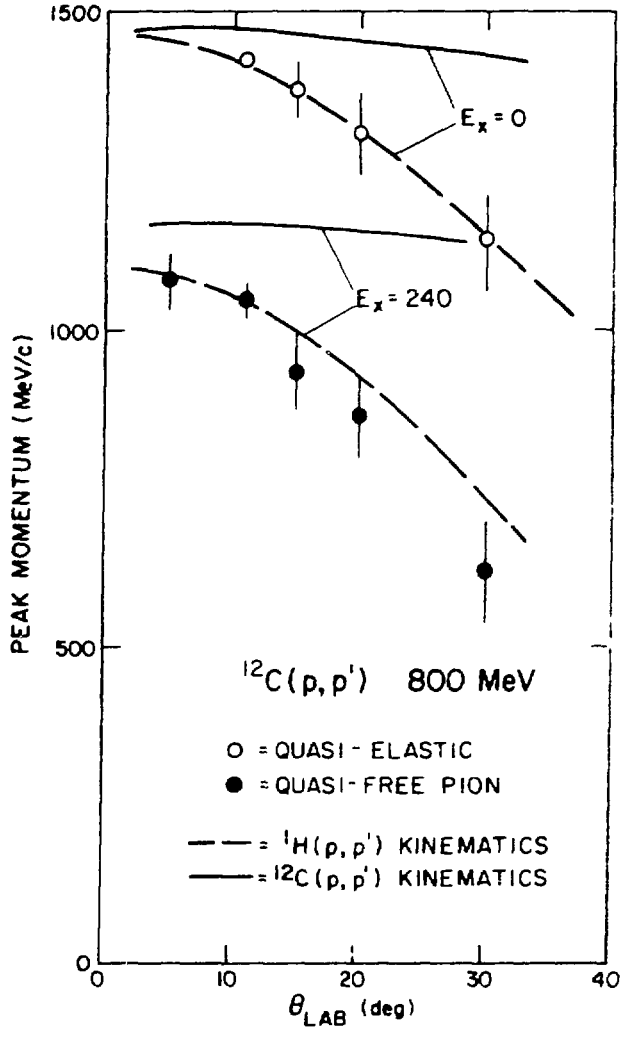

Figure 4.4: Momentum of the peaks in Figure 3.7 as a function of angle. Curves are the solution to the relativistic kinematics for the scattering of 800 MeV protons from ^{12}C (solid line) and ^{1}H (broken line).

Thus the evidence is good that the cross sections for p + nucleus scattering to very high energy losses are dominated by p + nucleon processes. The $\frac{d^2\sigma}{d\Omega dp}$ data have been divided into two regions, corresponding to quasi-elastic scattering and quasi-free pion production, and integrated over momentum, giving the angular distributions shown in Figures 4.5-4.8. Extrapolating the $\frac{d\sigma}{d\Omega}$ points out to $\theta_{lab} \approx 60^{o}$ (dashed line) and integrating over angle yields an estimate of the total cross section for nucleon-nucleon processes in nuclei. The results of this integration are given in Table 4.1, along with the measured values for the total reaction cross section, and Optical Model predictions for the total reaction cross section obtained using the KHT microscopic optical potential[35].

C: CONCLUSIONS:

The information in Table 4.1 indicates that as much as 65 % of the 800 MeV p + nucleus reaction cross section may be explained in terms of nucleon-nucleon processes. However the conclusions to be drawn from the comparison of total reaction cross sections with the angle- and momentum-integrated $\frac{d^2\sigma}{d\Omega dp}$ are in general less obvious for the heavier nuclei (^{40}Ca and ^{208}Pb) than for ^{2}H and ^{12}C. First, the $\frac{d^2\sigma}{d\Omega dp}$ data for the heavier nuclei do not drop off as rapidly as the lighter nuclei at small outgoing momenta, so that the strength omitted by cutting off the integration at ~ 300 MeV/c is larger. And second, the angular distributions that result from the momentum integration are more sensitive to the particular extrapolation assumed for angles

CROSS SECTION (mb)

Target	Quasi-elastic	Quasi-free π	Total	KMT	Measured
^{1}H	25.1 ± 1.2	19.7 ± 1.7	44.8 ± 2.1	47.3	---
^{2}H	---	34.9 ± 1.7	---	---	---
^{12}C	87 ± 5	137 ± 7	224 ± 9	269	278 ± 9
^{40}Ca	208 ± 12	335 ± 24	543 ± 27	615	622 ± 32
^{208}Pb	294 ± 12	825 ± 49	1119 ± 52	1800	1836 ± 212

TABLE 4.1: Contributions of the integrated Quasi-elastic region and the Quasi-free pion production region to the reaction cross section. The KMT calculation is from Ref. 35. The total reaction cross section measured in Experiment 386 (discussed in the text) is also given.

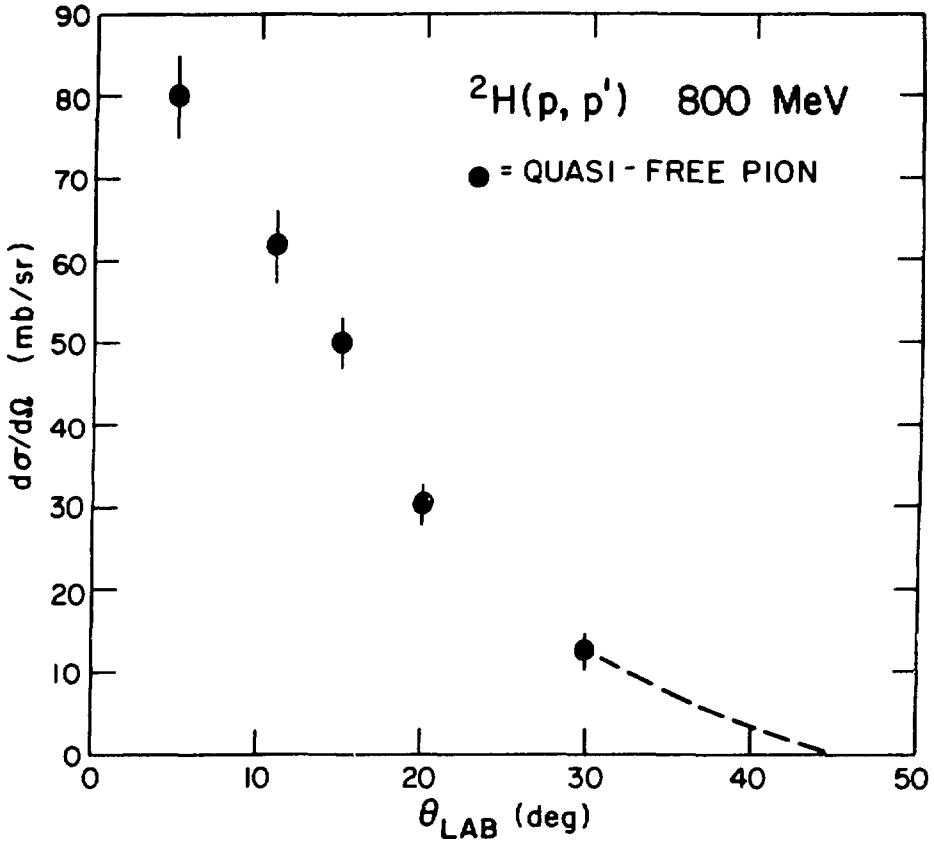

Figure 4.5: Angular distribution of the total pion production contribution to the ^{2}H(p,p') spectrum in Figure 3.6.

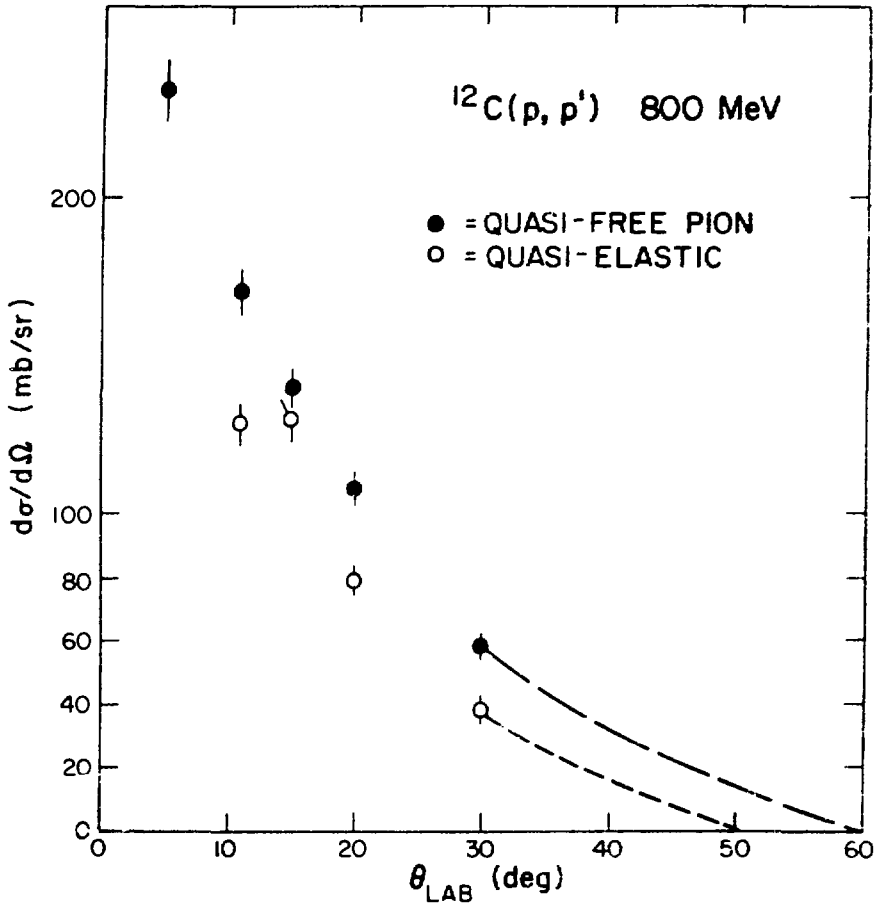

Figure 4.6: Angular distribution of the total quasi-elastic cross section (open circles) and the total quasi-free pion production cross section (solid dots) for p + ^{12}C scattering.

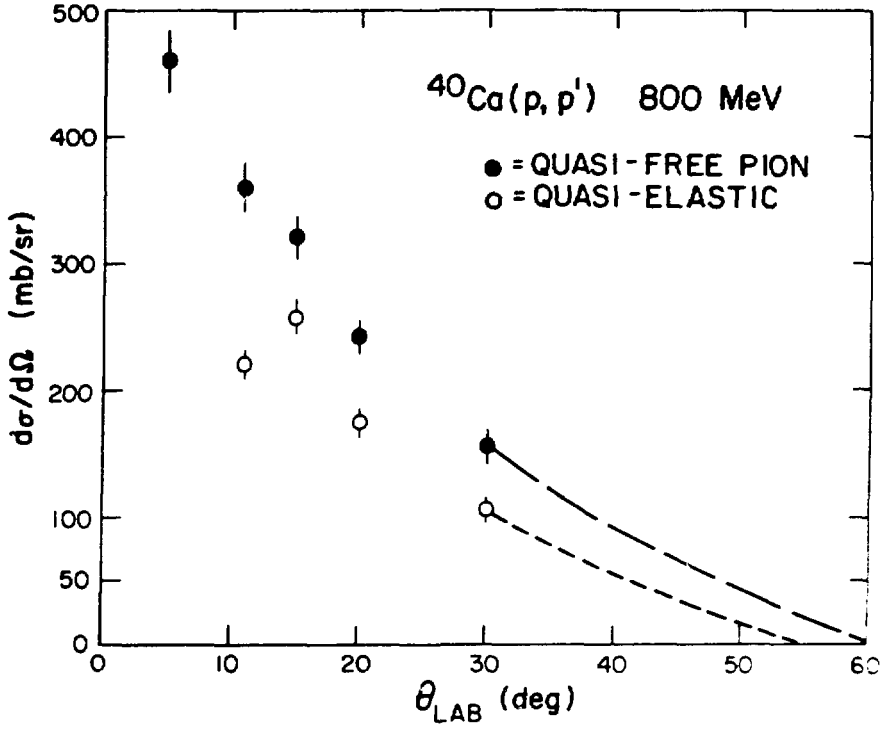

Figure 4.7: Same as Figure 4.6, for p + ^{40}Ca.

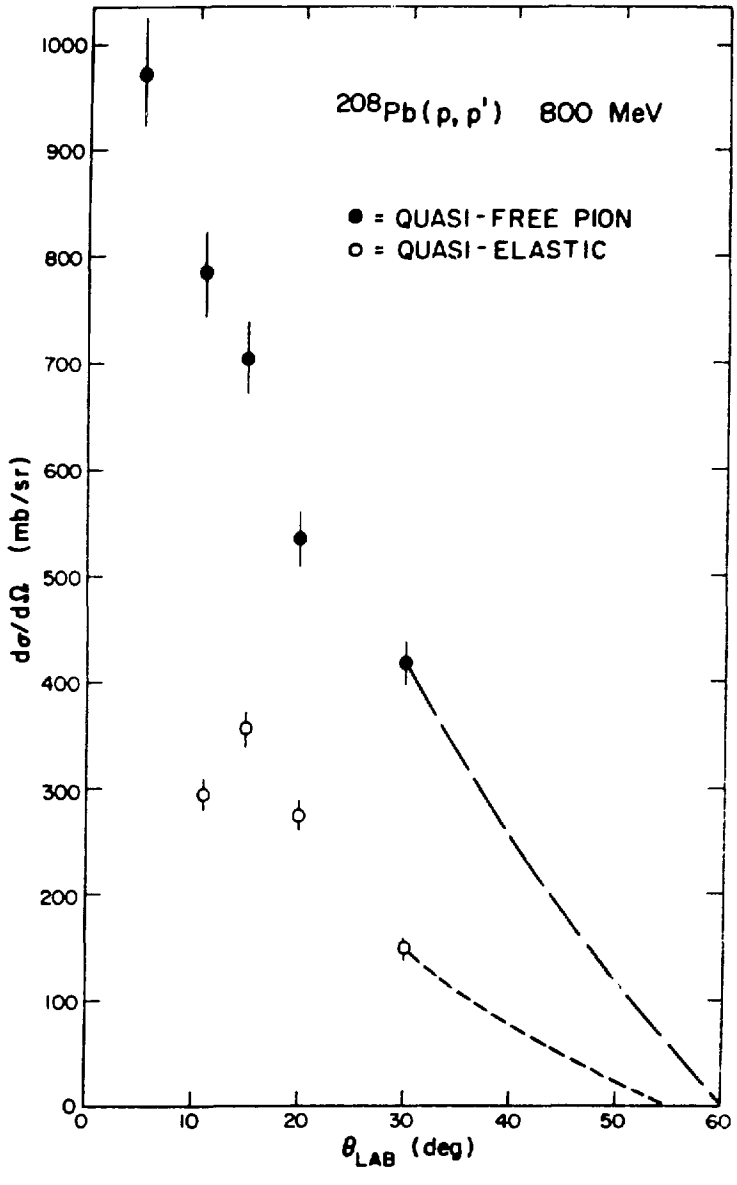

Figure 4.8: Same as Figure 4.6, for p + ^{208}Pb.

greater than 30^{o} in the lab. Alternately for ^{2}H and ^{12}C the integrated cross section at momenta below ~ 300 MeV/c is small, and the angular distributions of both the quasi-elastic and the quasi-free pion production regions are sufficiently small at $\theta_{lab} = 30^{o}$ to be relatively insensitive to the extrapolation used to larger angles. These problems, of course, can be accomodated by measuring the experimental cross sections to lower outgoing momenta and larger angles. Such an experiment is scheduled in the coming months. However providing this data will not make the association of that cross section with nucleon-nucleon processes more apparent.

The basis for our conclusion that only nucleon-nucleon reactions lead to the reaction cross section is the kinematical similarity between the p + nucleus data and the p + p data. Based on this similarity for light nuclei the Quasi-free Doorway Model[36] has been discussed, in which the higher-multiplicity reactions are assumed to evolve from an initial nucleon-nucleon interaction. Predictions of the $^{12}C(p,p')$ spectra have been published for a plane-wave calculation. Calculations which include the distorting effects of the nuclear medium are currently underway. The ability of the theory to reproduce the data for heavier nuclei will provide a good test of the Quasi-free Doorway Model.

D: SUMMARY

We have presented data for A(p,p′)X inclusive cross sections at 800 MeV, and have attempted to associate those inclusive data with nucleon-nucleon processes in nuclei. Such an association appears valid for light nuclei, but is less obvious for heavier nuclei. Accordingly we have found that as much as 80- 85 % of 800 MeV p + nucleus reactions in light nuclei proceed from nucleon-nucleon interactions in the nucleus, supporting the use of the impulse approximation for practical applications of Multiple Scattering theories. The case for heavier nuclei must await further experimental and theoretical developments.

APPENDIX A

SYNOPSIS OF DATA FOR EXPERIMENT 470

A synopsis of the data taken in Experiment 470 is given here. Refer to the text for a further description of the analysis.

	θ_{lab}	P_{sp}	n_{tgt} (nuclei/mb)	$\frac{d^2\sigma}{d\Omega dp}$ (mb/sr/MeV/c)
^4H (p,p')				
	5°	350	3.98×10^{-5}	.0119 ± .0018
	5°	400	3.98×10^{-5}	.0168 ± .0024
	5°	480	3.98×10^{-5}	.0324 ± .0032
	5°	680	3.98×10^{-5}	.0559 ± .0046
	5°	780	3.98×10^{-5}	.0680 ± .0053
	5°	880	3.98×10^{-5}	.0486 ± .0060
	5°	980	3.98×10^{-5}	.0985 ± .0071
	5°	1180	3.98×10^{-5}	.0823 ± .0067
	5°	1260	3.98×10^{-5}	.0110 ± .0031
	5°	1320	3.98×10^{-5}	.0036 ± .0030
	5°	1380	3.98×10^{-5}	.0000 ± .0062
	11°	350	3.98×10^{-5}	.0130 ± .0019
	11°	400	3.98×10^{-5}	.0202 ± .0021
	11°	450	3.98×10^{-5}	.0237 ± .0026
	11°	550	3.98×10^{-5}	.0356 ± .0032
	11°	650	3.98×10^{-5}	.0432 ± .0035
	11°	750	3.98×10^{-5}	.0588 ± .0041
	11°	850	3.98×10^{-5}	.0607 ± .0046
	11°	950	3.98×10^{-5}	.0743 ± .0055
	11	1050	$3.98\ 10^{-5}$	.0747 ± .0057
	11°	1120	3.98×10^{-5}	.0674 ± .0049
	11°	1200	3.98×10^{-5}	.0280 ± .0028
	11°	1240	3.98×10^{-5}	.0022 ± .0021
	11°	1280	3.98×10^{-5}	.0000 ± .0030
	11°	1350	3.98×10^{-5}	.0180 ± .0093
	15°	340	LH_2	.0104 ± .0006
	15°	380	LH_2	.0139 ± .0008
	15°	453	LH_2	.0178 ± .0011
	15°	527	LH_2	.0262 ± .0015
	15°	601	LH_2	.0322 ± .0019
	15°	676	LH_2	.0366 ± .0021
	15°	752	LH_2	.0417 ± .0025
	15°	829	LH_2	.0473 ± .0028
	15°	898	LH_2	.0565 ± .0033
	15°	975	LH_2	.0604 ± .0036

	θ_{lab}	P_{sp}	n_{tgt} (nuclei/mb)	$\frac{d^2\sigma}{d\Omega dp}$ (mb/sr/MeV/c)
^1H (p,p')	cont'd			
	15°	1049	LH_2	.0531 ± .0032
	15°	1125	LH_2	.0310 ± .0019
	15°	1150	LH_2	.0195 ± .0012
	15°	1176	LH_2	.0045 ± .0003
	15°	1202	LH_2	.0009 ± .0002
	15°	1229	LH_2	.0011 ± .0003
	20°	340	LH_2	.0119 ± .0015
	20°	380	LH_2	.0141 ± .0017
	20°	484	LH_2	.0185 ± .0010
	20°	601	LH_2	.0219 ± .0013
	20°	860	LH_2	.0334 ± .0022
	20°	1010	LH_2	.0237 ± .0014
	20°	1160	LH_2	.00096 ± .00005
	25°	340	LH_2	.0114 ± .0007
	25°	380	LH_2	.0148 ± .0010
	25°	480	LH_2	.0170 ± .0011
	25°	630	LH_2	.0215 ± .0013
	25°	780	LH_2	.0221 ± .0013
	25°	930	LH_2	.0140 ± .0009
	25°	1000	LH_2	.0057 ± .0003
	25°	1080	LH_2	.00047 ± .00003
	30°	340	LH_2	.0120 ± .0007
	30°	375	LH_2	.0136 ± .0008
	30°	426	LH_2	.0133 ± .0008
	30°	550	LH_2	.0161 ± .0009
	30°	700	LH_2	.0142 ± .0008
	30°	850	LH_2	.0072 ± .0005
	30°	925	LH_2	.0020 ± .0002
	30°	1000	LH_2	.00033 ± .00015
	30°	1067	LH_2	.0000 ± .0003
^2H (p,p')				
	5°	350	3.58×10^{-5}	.020 ± .002
	5°	400	3.58×10^{-5}	.026 ± .003
	5°	480	3.58×10^{-5}	.043 ± .003
	5°	580	3.58×10^{-5}	.051 ± .004
	5°	680	3.58×10^{-5}	.070 ± .005
	5°	780	3.58×10^{-5}	.099 ± .006
	5°	880	3.58×10^{-5}	.098 ± .005
	5°	980	3.58×10^{-5}	.144 ± .008
	5°	1080	3.58×10^{-5}	.154 ± .009
	5°	1180	3.58×10^{-5}	.102 ± .007
	5°	1260	3.58×10^{-5}	.031 ± .004
	5°	1320	3.58×10^{-5}	.025 ± .003
	5°	1380	3.58×10^{-5}	.050 ± .007

	θ_{lab}	P_{sp}	n_{tgt} (nuclei/mb)	$\frac{d^2\sigma}{d\Omega dp}$ (mb/sr/MeV/c)
^2H (p,p')	cont'd			
	11°	350	3.58×10^{-5}	.024 ± .003
	11°	400	3.58×10^{-5}	.032 ± .006
	11°	450	3.58×10^{-5}	.031 ± .004
	11°	550	3.58×10^{-5}	.047 ± .003
	11°	650	3.58×10^{-5}	.063 ± .004
	11°	750	3.58×10^{-5}	.081 ± .005
	11°	850	3.58×10^{-5}	.075 ± .005
	11°	950	3.58×10^{-5}	.110 ± .006
	11°	1050	3.58×10^{-5}	.116 ± .007
	11°	1120	3.58×10^{-5}	.089 ± .005
	11°	1200	3.58×10^{-5}	.044 ± .003
	11°	1240	3.58×10^{-5}	.029 ± .002
	11°	1280	3.58×10^{-5}	.017 ± .003
	11°	1350	3.58×10^{-5}	.115 ± .011
	11°	1414	3.58×10^{-5}	1.388 ± .060
	15°	340	3.58×10^{-5}	.015 ± .002
	15°	450	3.58×10^{-5}	.030 ± .003
	15°	600	3.58×10^{-5}	.055 ± .004
	15°	750	3.58×10^{-5}	.079 ± .005
	15°	900	3.58×10^{-5}	.091 ± .006
	15°	1050	3.58×10^{-5}	.079 ± .006
	15°	1200	3.58×10^{-5}	.023 ± .003
	15°	1374	3.58×10^{-5}	1.017 ± .060
	20°	350	3.58×10^{-5}	.022 ± .002
	20°	420	3.58×10^{-5}	.029 ± .002
	20°	520	3.58×10^{-5}	.034 ± .003
	20°	620	3.58×10^{-5}	.040 ± .003
	20°	720	3.58×10^{-5}	.049 ± .003
	20°	820	3.58×10^{-5}	.052 ± .003
	20°	920	3.58×10^{-5}	.049 ± .003
	20°	1020	3.58×10^{-5}	.037 ± .003
	20°	1080	3.58×10^{-5}	.022 ± .002
	20°	1120	3.58×10^{-5}	.015 ± .002
	20°	1160	3.58×10^{-5}	.013 ± .003
	20°	1230	3.58×10^{-5}	.071 ± .006
	20°	1310	3.58×10^{-5}	.534 ± .021
	30°	340	3.58×10^{-5}	.013 ± .003
	30°	380	3.58×10^{-5}	.018 ± .003
	30°	500	3.58×10^{-5}	.021 ± .002
	30°	650	3.58×10^{-5}	.029 ± .003
	30°	800	3.58×10^{-5}	.021 ± .002
	30°	925	3.58×10^{-5}	.015 ± .002
	30°	1001	3.58×10^{-5}	.015 ± .002
	30°	1145	3.58×10^{-5}	.131 ± .007

	θ_{lab}	P_{sp}	n_{tgt} (nuclei/mb)	$\frac{d^2\sigma}{d\Omega dp}$ (mb/sr/MeV/c)
^{12}C (p,p')				
	5°	350	8.73×10^{-6}	.079 ± .004
	5°	400	8.73×10^{-6}	.103 ± .005
	5°	480	8.73×10^{-6}	.131 ± .006
	5°	580	8.73×10^{-6}	.173 ± .008
	5°	680	8.73×10^{-6}	.212 ± .009
	5°	780	8.73×10^{-6}	.241 ± .010
	5°	880	8.73×10^{-6}	.275 ± .011
	5°	980	8.73×10^{-6}	.329 ± .014
	5°	1080	8.73×10^{-6}	.408 ± .017
	5°	1180	8.73×10^{-6}	.348 ± .014
	5°	1260	8.73×10^{-6}	.184 ± .006
	5°	1320	8.73×10^{-6}	.175 ± .008
	5°	1380	8.73×10^{-6}	.392 ± .016
	11°	350	8.73×10^{-6}	.101 ± .004
	11°	400	8.73×10^{-6}	.108 ± .005
	11°	450	8.73×10^{-6}	.133 ± .006
	11°	550	8.73×10^{-6}	.156 ± .006
	11°	650	8.73×10^{-6}	.182 ± .007
	11°	750	8.73×10^{-6}	.204 ± .008
	11°	850	8.73×10^{-6}	.231 ± .009
	11°	950	8.73×10^{-6}	.240 ± .010
	11°	1050	8.73×10^{-6}	.263 ± .011
	11°	1120	8.73×10^{-6}	.227 ± .009
	11°	1200	8.73×10^{-6}	.152 ± .006
	11°	1240	8.73×10^{-6}	.137 ± .006
	11°	1280	8.73×10^{-6}	.158 ± .007
	11°	1350	8.73×10^{-6}	.618 ± .025
	11°	1414	8.73×10^{-6}	1.709 ± .069
	15°	340	2.30×10^{-6}	.084 ± .006
	15°	450	2.30×10^{-6}	.115 ± .006
	15°	600	2.30×10^{-6}	.157 ± .008
	15°	750	2.30×10^{-6}	.186 ± .010
	15°	900	2.30×10^{-6}	.204 ± .011
	15°	1050	2.30×10^{-6}	.196 ± .010
	15°	1200	2.30×10^{-6}	.150 ± .008
	15°	1374	2.30×10^{-6}	.980 ± .048
	20°	350	8.73×10^{-6}	.098 ± .005
	20°	420	8.73×10^{-6}	.115 ± .006
	20°	520	8.73×10^{-6}	.129 ± .006
	20°	620	8.73×10^{-6}	.141 ± .007
	20°	720	8.73×10^{-6}	.146 ± .007
	20°	820	8.73×10^{-6}	.149 ± .007
	20°	920	8.73×10^{-6}	.149 ± .007
	20°	1020	8.73×10^{-6}	.134 ± .007
	20°	1080	8.73×10^{-6}	.124 ± .006

	θ_{lab}	P_{sp}	n_{tgt} (nuclei/mb)	$\frac{d^2\sigma}{d\Omega dp}$ (mb/sr/MeV/c)
^{12}C (p,p')	cont'd			
	20°	1120	8.73×10^{-6}	.133 ± .007
	20°	1160	8.73×10^{-6}	.169 ± .008
	20°	1230	8.73×10^{-6}	.316 ± .016
	20°	1310	8.73×10^{-6}	.449 ± .021
	30°	340	2.30×10^{-6}	.077 ± .005
	30°	380	2.30×10^{-6}	.086 ± .006
	30°	500	2.30×10^{-6}	.103 ± .005
	30°	650	2.30×10^{-6}	.106 ± .006
	30°	800	2.30×10^{-6}	.099 ± .005
	30°	925	2.30×10^{-6}	.099 ± .005
	30°	1000	2.30×10^{-6}	.116 ± .006
	30°	1145	2.30×10^{-6}	.149 ± .008
^{40}Ca (p,p')				
	5°	350	2.19×10^{-6}	.262 ± .012
	5°	400	2.19×10^{-6}	.310 ± .013
	5°	461	2.19×10^{-6}	.356 ± .016
	5°	580	2.19×10^{-6}	.369 ± .019
	5°	680	2.19×10^{-6}	.426 ± .021
	5°	780	2.19×10^{-6}	.505 ± .023
	5°	880	2.19×10^{-6}	.493 ± .023
	5°	980	2.19×10^{-6}	.575 ± .026
	5°	1080	2.19×10^{-6}	.704 ± .032
	5°	1180	2.19×10^{-6}	.644 ± .026
	5°	1260	2.19×10^{-6}	.357 ± .016
	5°	1320	2.19×10^{-6}	.306 ± .015
	5°	1389	2.19×10^{-6}	.641 ± .038
	11°	350	2.19×10^{-6}	.334 ± .014
	11°	400	2.19×10^{-6}	.332 ± .014
	11°	450	2.19×10^{-6}	.377 ± .016
	11°	550	2.19×10^{-6}	.389 ± .017
	11°	650	2.19×10^{-6}	.403 ± .017
	11°	750	2.19×10^{-6}	.431 ± .018
	11°	850	2.19×10^{-6}	.443 ± .019
	11°	950	2.19×10^{-6}	.466 ± .020
	11°	1050	2.19×10^{-6}	.476 ± .020
	11°	1120	2.19×10^{-6}	.423 ± .018
	11°	1200	2.19×10^{-6}	.311 ± .013
	11°	1240	2.19×10^{-6}	.268 ± .012
	11°	1280	2.19×10^{-6}	.277 ± .012
	11°	1350	2.19×10^{-6}	1.024 ± .044
	11°	1414	2.19×10^{-6}	2.80 ± .11
	15°	340	7.29×10^{-7}	.268 ± .020
	15°	450	7.29×10^{-7}	.330 ± .018
	15°	600	7.29×10^{-7}	.405 ± .021
	15°	750	7.29×10^{-7}	.405 ± .022

	θ_{lab}	P_{sp}	n_{tgt} (nuclei/mb)	$\frac{d\sigma}{d\Omega}$ (mb/sr/MeV)
^{40}Ca (p,p')	cont'd			
	15°	900	7.29×10^{-7}	.42 ± .23
	15°	1050	7.29×10^{-7}	.39 ± .
	15°	1200	7.29×10^{-7}	. ± .
	15°	1374	7.29×10^{-7}	1. ± .9
	20°	35	2.19×10^{-6}	. ± .
	20°	42	2.19×10^{-6}	. ± .
	20°	52	2.19×10^{-6}	. ± .
	20°	62	2.19×10^{-6}	. ± .
	20°	72	2.19×10^{-6}	.334 ± .14
	20°	82	2.19×10^{-6}	.317 ± .013
	20°	92	2.19×10^{-6}	. ± .
	25°	1	2.19×10^{-6}	.27 ± .
	25°	1	2.19×10^{-6}	.24 ± .
	25°	1	2.19×10^{-6}	.241 ± .
	25°	1	2.19×10^{-6}	.292 ± .
	25°	1	2.19×10^{-6}	. ± .
	25°	1	2.19×10^{-6}	. ± .
	30°	34	7.29×10^{-7}	.255 ± .18
	30°	38	7.29×10^{-7}	.298 ± .
	30°	500	7.29×10^{-7}	.285 ± .
	30°	650	7.29×10^{-7}	.296 ± .
	30°	800	7.29×10^{-7}	. ± .
	30°	925	7.29×10^{-7}	. ± .
	30°	1000	7.29×10^{-7}	. ± .
	30°	1145	7.29×10^{-7}	. ± .
^{208}Pb (p,p')				
	5°	350	4.37×10^{-7}	.829 ± .042
	5°	400	4.37×10^{-7}	.942 ± .
	5°	480	4.37×10^{-7}	.916 ± .050
	5°	580	4.37×10^{-7}	.925 ± .
	5°	680	4.37×10^{-7}	.911 ± .
	5°	780	4.37×10^{-7}	.991 ± .051
	5°	880	4.37×10^{-7}	1.022 ± .050
	5°	980	4.37×10^{-7}	1.099 ± .052
	5°	1080	4.37×10^{-7}	1.327 ± .059
	5°	1180	4.37×10^{-7}	1.196 ± .053
	5°	1260	4.37×10^{-7}	.792 ± .038
	5°	1320	4.37×10^{-7}	.606 ± .034
	5°	1380	4.37×10^{-7}	2.547 ± .110
	11°	350	4.37×10^{-7}	1.05 ± .04
	11°	400	4.37×10^{-7}	1.04 ± .04
	11°	450	4.37×10^{-7}	1.02 ± .04
	11°	550	4.37×10^{-7}	.93 ± .04
	11°	650	4.37×10^{-7}	.92 ± .04
	11°	750	4.37×10^{-7}	.92 ± .04

	θ_{lab}	E_{sp}	n_{tgt} (nuclei/cm^2)	$\frac{d\sigma}{d\omega_i}$ (mb/sr/mole/e$^-$)
^{206}Pb(p,p')	cont'd			
	11°	85[illegible]	[illegible]	.[illegible] ± .[illegible]
	11°	95[illegible]	[illegible]	.[illegible] ± .[illegible]
	11°	1[illegible]	[illegible]	.[illegible] ± .[illegible]
	11°	112[illegible]	[illegible]	.[illegible] ± .[illegible]
	11°	120[illegible]	[illegible]	.[illegible] ± .[illegible]
	11°	124[illegible]	[illegible]	.[illegible] ± .[illegible]
	11°	128	[illegible]	.[illegible] ± .[illegible]
	11°	135	[illegible]	1.[illegible] ± .[illegible]
	11°	1[illegible]	[illegible]	[illegible] ± [illegible]
	15°	34	[illegible]	.[illegible] ± .[illegible]
	15°	45	[illegible]	.[illegible] ± .[illegible]
	15°	6[illegible]	[illegible]	.[illegible] ± .[illegible]
	15°	7[illegible]	[illegible]	.[illegible] ± .[illegible]
	15°	9[illegible]	[illegible]	.[illegible] ± .[illegible]
	15°	[illegible]	[illegible]	.[illegible] ± .[illegible]
	15°	12[illegible]	[illegible]	.[illegible] ± .[illegible]
	15°	13[illegible]	[illegible]	[illegible] ± [illegible]
	20°	55[illegible]	[illegible]	1.[illegible] ± .[illegible]
	20°	62	[illegible]	.[illegible] ± .[illegible]
	20°	72	[illegible]	.[illegible] ± .[illegible]
	20°	82[illegible]	[illegible]	.[illegible] ± .[illegible]
	20°	92[illegible]	[illegible]	.[illegible] ± .[illegible]
	20°	1[illegible]20	[illegible]	.[illegible] ± .[illegible]
	20°	1[illegible]80	[illegible]	.[illegible] ± .[illegible]
	20°	112[illegible]	[illegible]	.[illegible] ± .[illegible]
	20°	118[illegible]	[illegible]	.[illegible] ± .[illegible]
	20°	123[illegible]	[illegible]	.[illegible] ± .[illegible]
	20°	131[illegible]	[illegible]	1.[illegible] ± .[illegible]
	30°	340	1.46×10^{-7}	.61 ± .07
	30°	381	1.46×10^{-7}	.91 ± .07
	30°	500	1.46×10^{-7}	.80 ± .09
	30°	650	1.46×10^{-7}	.65 ± .04
	30°	800	1.46×10^{-7}	.49 ± .03
	30°	925	1.46×10^{-7}	.41 ± .03
	30°	1000	1.46×10^{-7}	.39 ± .02
	30°	1145	1.46×10^{-7}	.53 ± .04

APPENDIX B

A FAST, LOW-MASS DETECTOR FOR CHARGED PARTICLES

by J. A. McGill, L. G. Atencio, and C. L. Morris

Nuclear Instruments and Methods (to be published)

Multi-wire proportional counters (MWPC) using delay lines and one amplifier per wire have been described in the literature. A good review of such counters is given in Reference 39, and references therein. In this paper we describe a MWPC designed to operate at significantly reduced gas pressures, and to provide position, time, and angle information. It presents a low mass to charged particles traversing it, and is intended to be used with a small beam. The specific detector described was built as an upstream profile monitor for an 800 MeV proton beam.

CONSTRUCTION and INSTALLATION

The body of the counter was machined from a 4" × $2\frac{1}{2}$" × 2" aluminum block as shown in Figure 61. A piece of 20 μm ϕ Au-plated tungsten wire (a) was strung down the center of each of the three $\frac{1}{2}$" bores, soldered at one end to a modified SHV connector (b). Prior to this each SHV connector had its solder tip cut back, and a 0.6mm hole was drilled therein at the geometric center of the threads. With the connector and wire installed, the other end of

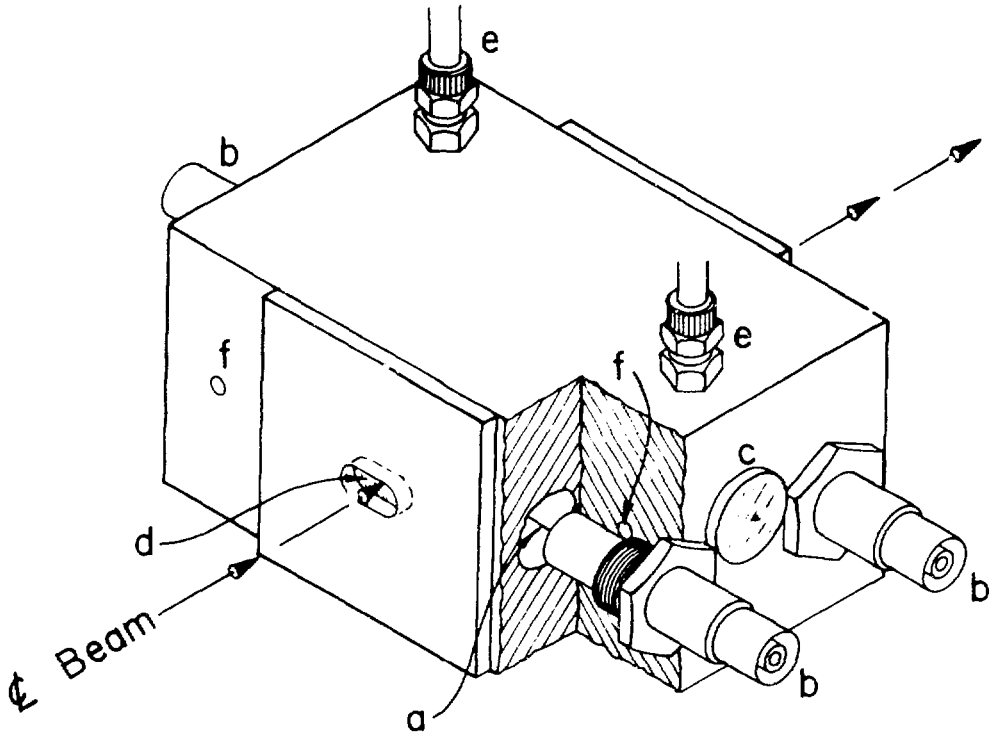

Figure B1: An assembly drawing of the chamber described, showing the position of an anode wire (a), SHV connectors (b), one of three lucite centering plugs (c), one of the 0.0005" mylar windows. Gas from the handling system entered through one of the $\frac{1}{4}$" poly-flo lines (e) and exitted the other, with cross-flow provided by the $\frac{1}{8}$" holes (f).

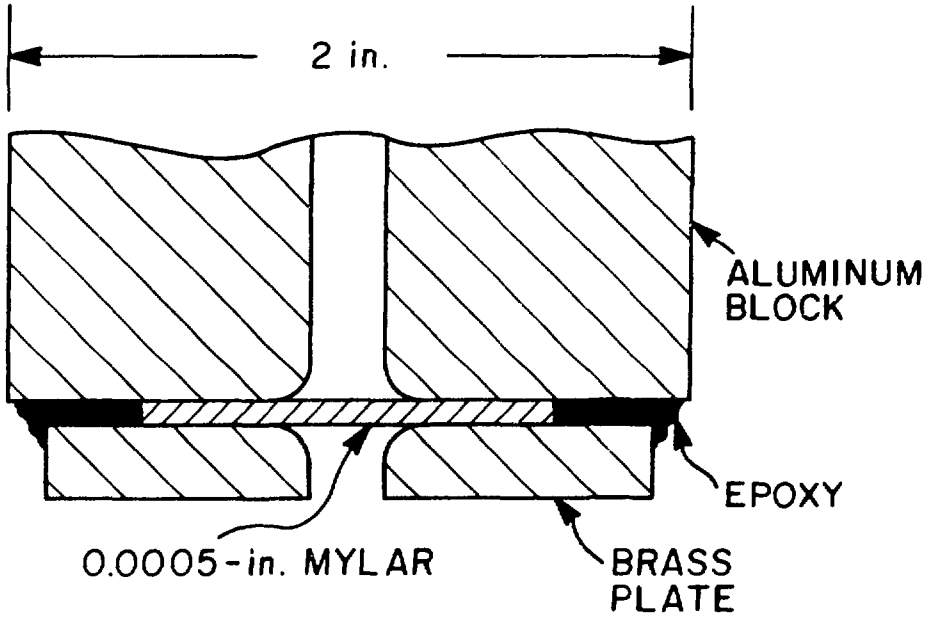

Figure B2: Detail of the interface between the chamber body, $\frac{1}{2}$ mil mylar window, and the brass plate.

the wire was threaded through a lucite centering plug (c), a 30 gm. tensioning weight was attached, and the wire and plug were secured with epoxy.

The oblong hole through the $2\frac{1}{2}$" dimension of the block was covered at each end with a .0005" Mylar window (d) sandwiched between a brass plate and the block. All edges were rounded and smeared with a light film of silicon grease to keep the epoxy at the perimeter of the Mylar, allowing the Mylar to flex without encountering any sharp edges (Figure B2).

Poly-flo fittings (Figure B1(e)) provided gas entry and exit, with cross-flow between wires through $\frac{1}{8}$" holes (f). These holes were plugged to the environment with epoxy. The gas handling system is shown in Figure B3. Gas pressure in the chamber is monitored by a 0-800 mm differential pressure gauge installed as shown. The Manostat used to regulate gas pressure was advertised as capable of maintaining a constant pressure over a wide range of thru-rates, but in reality some adjusting was necessary to achieve a specific combination of flow and pressure. However once set, the Manostat was quite stable over periods of up to 72 hrs.

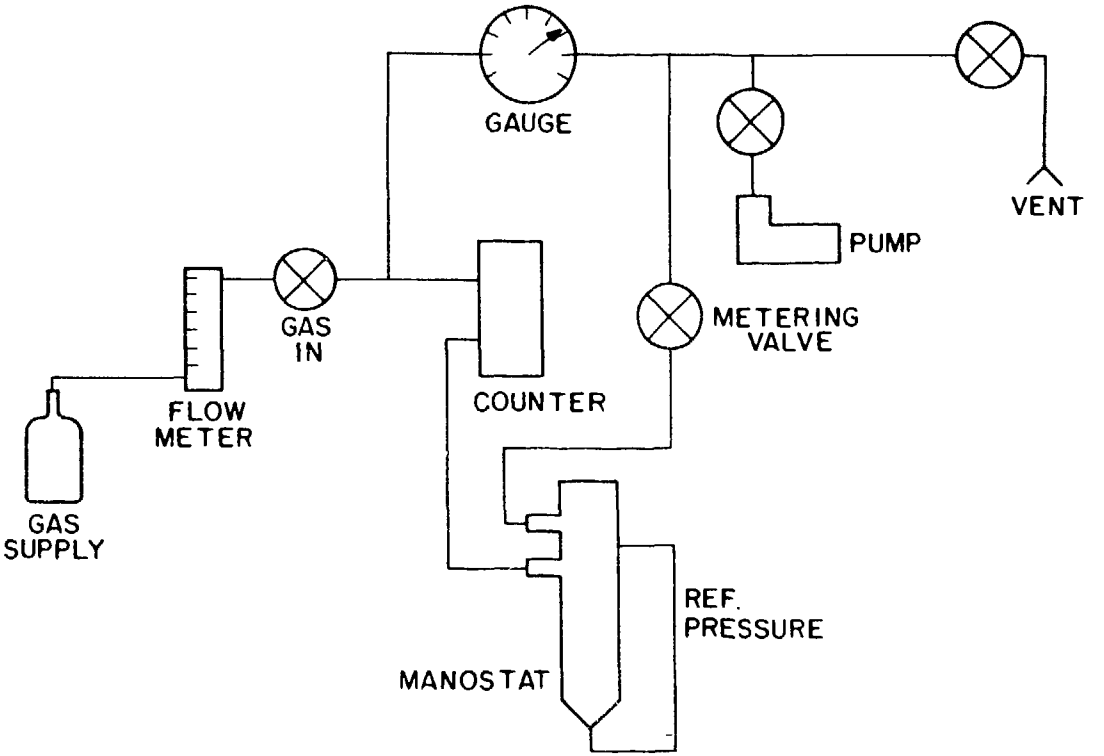

Figure B3: The vacuum gas handling system used in the operation of the counter. Once reference pressure was set, flow rate and pressure remained steady for days.

TIMING and POSITION INFORMATION

A reference coordinate system is shown in Figure B4. The distances x_1, x_2, and x_3 are assumed to have a linear relationship with drift time,

$$x_j = (t_j - t_o)v \quad , \tag{B.1}$$

where t_o is the time the particle passes through the chamber, t_j is the arrival time of the pulse from the i^{th} anode, and v is the drift velocity (approx 20ns/mm). Further, relations for position and angle are

$$x = \ell - x_2 = \frac{x_3 + x_1}{2} \quad \text{and} \tag{B.2}$$

$$\theta = \frac{x_3 - x_1}{2d} \quad . \tag{B.3}$$

Combining (B.1) and (B.2) yields

$$t_o + \frac{\ell}{2v} = \frac{1}{4}(t_3 + t_1 + 2t_2) \quad . \tag{B.4}$$

So t_o corresponds to the time a particle passes the midplane of the detector. The constant $\frac{\ell}{2v}$ can be treated as an offset, and removed with delay lines in the timing circuit. Similarly,

$$x - \ell = (t_o - t_2)v \tag{B.5}$$

$$\theta = \frac{v}{2d}(t_3 - t_1) \quad . \tag{B.6}$$

Equations (B.4), (B.5), and (B.6) are the expressions for the three quantities available. t_o can be measured in a variety of ways, but

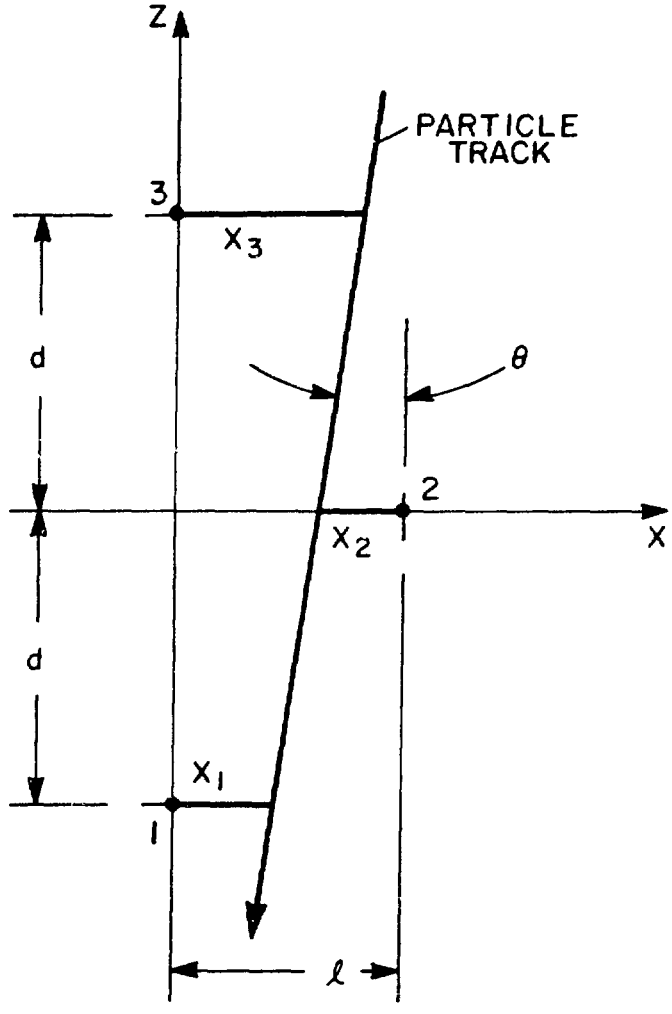

Figure B4: A reference coordinate system for the discussion in the text.

the most straitforward is to use a meantimer, eg. Lecroy Research Corp. model # 624, to obtain

$$\overline{t_1 t_2} = \frac{t_1 + t_2}{2}$$

Then

$$t_o = \overline{(t_1 t_2)(t_2 t_3)} + \text{offset} \quad .$$

The time differences can be calculated using TAC's or TDC's, and added together either with summing amplifiers or in software to obtain the other quantities.

RESULTS

Some plateau curves as a function of pressure are shown in Figure B5. For minimum ionizing particles, the device appears to be useful at pressures above 180 mm_{Hg} abs. Below these pressures anode efficiencies are less than 80%, and the plateau shoulder is too narrow to trust. At 300 mm_{Hg} the counter is ~ 7 mg/cm^2 thick, including the $\frac{1}{2}$ mil Mylar windows. The drift spectra in Figure B6 were taken with a ^{207}Bi source collimated to ~ 6mm. The drift velocities do not change measurably over a wide range of pressures, but stay constant at 20ns/mm.

In several trials with an 800 MeV proton beam, raw signals from the chamber had ~ 5mv amplitudes with 2ns rise times, when terminated into 50 Ω. By placing a scintillator directly behind the counter, the time resolution between the scintillator and t_o was measured to be 2 ns FWHM. The ultimate position resolution is expected to be ~0.1 mm based on previous drift chamber

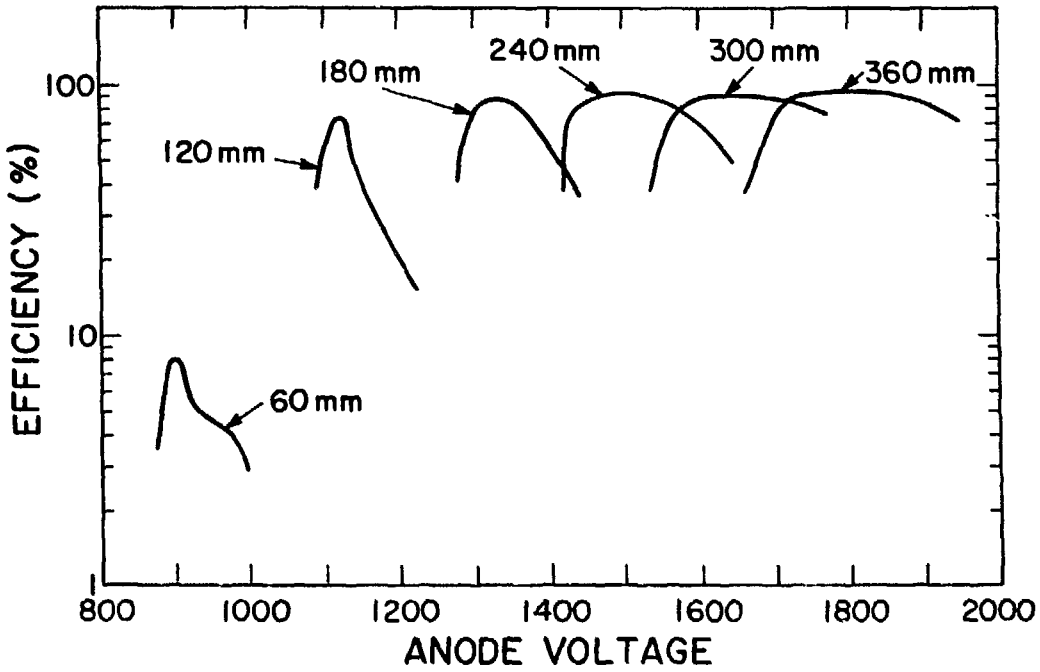

Figure B5: Plateau curves for various gas pressures. The efficiency of the entire counter is shown ($\nu = \nu_1 \cdot \nu_2 \cdot \nu_3$).

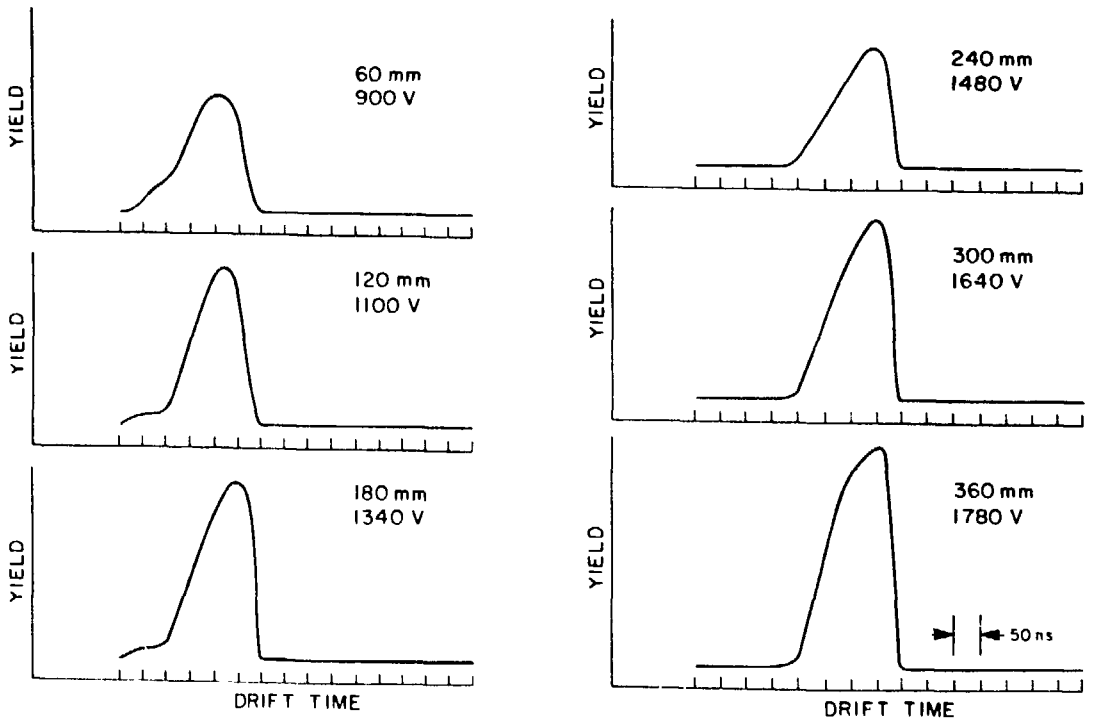

Figure 36: Typical drift spectra for different gas pressures. Absolute scale is arbitrary; divisions shown are 50 ns.

measurements[39]. Based on the position resolution one should be able to obtain an angle resolution of ~4 mrad with the present counter.

The counting-rate performance of the counter is limited by space charge effects, and consequently depends upon the beam spot size. Problems are expected to arise at counting rates exceeding 10^4/ linear mm of wire/ sec.

CONCLUSION

We have reported a small counter which presents a mass of 7 mg/cm^2 to incident particles and is capable of providing time, position, and angle information. Initial studies have shown it is possible to obtain better than 2 ns FWHM time resolution. Expected position resolutions are 0.1 mm and expected angle resolutions are 4 mrad.

Appendix C

Listed below is the Test Descriptor file used in Experiment 470.

```
601,65,55,4,            ;[165,76]ERS470.TST  CYCLE 25  DEC 1979
BOX 1,                  ;1 INSIDE BOX -- 1 , PID
BOX 2,                  ;2               2
BOX 3,                  ;3               3
1OR,-1,1,               ;4 LOOP 1 COUNTER
END,
GATE 1 1,-1,            ;5 SPARE
GATE 1,1,-1,            ;6 SPARE
GATE 1,1,-1,            ;7 SPARE
GATE 1,1,-1,            ;8 SPARE
GATE 12,20,600,         ;9 NORM
GATE 13,20,600,         ;10 REVERSE
B1,2,6,                 ;11 SPARE
B1,2,7,                 ;12 SPARE
CA,141,9871,10155,      ;13 CHMBR 1 CHKSUM
CA,142,9900,10100,      ;14       2
CA,143,9900,10100,      ;15       3
CA,144,9900,10100,      ;16       4
CA,145,9900,10100,      ;17       5
CA,146,9887,10169,      ;18       6
BOX 4,                  ;19 ANGLE CUT=> X(#185) VS ROTATED ANGLE (#196)
CA,239,9980,10020,      ;20 DRF DIFF 23 (+/- 2MM)
CA,240,9980,10020,      ;21 DRF DIFF 45 (+/- 2MM)
CA,185,8500,11500,      ;22 X DRIFT CHAMBERS
CA,181,13000,7000,      ;23 SPARE
IGAT 1,                 ;24 PEAK        1
IGAT 2,                 ;25             2
IGAT 3,                 ;26             3
IGAT 4,                 ;27             4
IGAT 5,                 ;28             5
CA 160,7500,12500,      ;29 CH2X
CA,148,9800,10200,      ;30 CH2Y
CA,162,7500,12500,      ;31 CH4X
CA,150,9800,10200,      ;32 CH4Y
BOX,5,                  ;33 BOX 5
BOX,6,                  ;34 BOX 6
BOX,7,                  ;35 BOX 7
BOX,8,                  ;36 BOX 8
BOX,9,                  ;37 BOX 9
CA,193,10020,10060,     ;38 SCATT ANGLE 1
CA,193,9985,10045,      ;39     "       2
CA,193,10045,10105,     ;40     "       3
CA,193,10105,10165,     ;41     "       4
CA,193,9872,10145,      ;42     "       5
CA,193,9890,10239,      ;43 FULL SCT ANGLE REGION 2 DEGREES
CA,181,13000,7000,      ;44 SPARE
CA,181,13000,7000,      ;45 SPARE
AND,-5,-6,              ;46 NOT JAWS
AND,-7,-8,              ;47 NOT VETOES
AND,46,47,              ;48 NOT ANTIS
AND,1,1,                ;49 GOOD PID => NO ANTIS, PID
AND,20,21,              ;50 DRF TST
AND,13,18,              ;51 DL OK
AND,14,15,16,17,        ;52 DR OK
AND,14,15,16,17,49,33,          ;53 DR CHMBRS, GOOD PID,BOX5
AND,14,15,16,17,49,50,  ;54 DR CHMBRS, GOOD PID, DRF TST
AND,20,33,49,52,                ;55 DR CBRS,GOOD PID,DRF23,BOX5
AND,21,33,49,52,                ;56 DR CHBRS,GOOD PID,DRF45,BOX5
AND,20,53,              ;57 TEST 53 AND DRF23
AND,21,53,              ;58 TEST 53 AND DRF45
AND,54,19,              ;59 GOOD EVENT => GOOD PID, DR CHS, XANGLE, DRF
AND,2,19,50,52,         ;60 GOOD BOX 2 EVENT
AND,15,16,17,49,21,33,  ;61 ALL DR CHMBRS BUT 2, GOOD PID, DRF45,BOX5
AND,14,16,17,49,21,33,  ;62                     3
AND,14,15,17,49,20,33,  ;63                     4               DRF23
AND,14,15,16,49,20,33,  ;64                     5
AND,3,19,50,52,         ;65 GOOD BOX 3 EVENT
```

```
AND,59,42,              ;66 GOOD EVENT, SCAT ANGLE 5
AND,59,34,38,           ;67 GOOD EVENT SCAT REG 1 THETATGT
AND,59,40,              ;68                       3
AND,59,41,              ;69                       4
AND,59,42,              ;70                       5
AND,59,24,              ;71 GOOD EVENT, PEAK 1
AND,59,24,34,           ;72 GOOD EVENT PEAK 1 THETA TGT
AND,59,26,              ;73                  3
AND,59,27,              ;74                  4
AND,59,28,              ;75                  5
AND,22,42,59,           ;76 X DRIFT CHAMBERS GOOD EVENT SCAT REGION 5
AND,35,59,              ;77 BOX 7 AND GOOD EVENT
AND,22,42,60,           ;78 X DRIFT CHAMBERS, GOOD EVENT BOX 2, SCATTERING ANGLE REGION 5
AND,22,42,65,           ;79 X DRIFT CHAMBERS, GOOD EVENT BOX 3, SCAT REGION 5
AND,22,59,              ;80 GOOD EVENT, X DRIFT CHAMBERS
AND,-16,17,49,          ;81 DRIFT 5, NOT 4, GOOD PID
AND,59,33,              ;82 GOOD EVENT, BOX 5
AND,59,34,              ;83                 6
AND,59,35,              ;84                 7
AND,59,36,              ;85                 8
AND 59,36,              ;86 GOOD EVENT BOX 8
AND,59,39,              ;87 GOOD EVENT, SCAT ANGLE  2
AND,59,40,              ;88                         3
AND,59,41,              ;89                         4
AND,59,42,              ;90                         5
AND,3,19,22,42,50,52        ;91   PID12 EQUIVALENT OF TEST 76
IOR,1,-1,               ;92 LOOP 2 COUNTER
END
FINISH
```

ACKNOWLEDGMENT

As is usually the case, those who have gone before have made straight the way for those who follow. In particular I am grateful to the LAMPF staff and users who have contributed to the hardware and software which facilitated the experiments described here. Special thanks go to Jim Amann for his fervent efforts. The collaborators on these experiments also rendered specific assistance, most notably Ray Ferguson, Cas Milner, and George Burleson. Martin Barlett not only collaborated in the collection of the data, but also in many hours of discussions and "thinking out loud." Of course Gerry Hoffmann, my thesis advisor, deserves my greatest appreciation for the help and guidance he has given throughout the last three years.

This work was supported by the Department of Energy and by The Robert A. Welch Foundation.

REFERENCES

1. K. M. Watson, Physical Review 89, 575 (1953).

2. N. C. Francis and K. M. Watson, Physical Review 92, 291 (1953).

3. W. B. Riesenfeld and K. M. Watson, Physical Review 102, 1157 (1956).

4. H. Feshbach in Annual Reviews of Nuclear Science, E. Segré, ed. vol. 8, 49 (1958).

5. S. Fernbach, R. Serber, and T. B. Taylor, Physical Review 75, 1352 (1949).

6. G. F. Chew, Physical Review 80, 196 (1950).

7. G. F. Chew and M. L. Goldberger, Physical Review 87, 778 (1952).

8. A. K. Kerman, M. McManus, and R. M. Thaler, Annals of Physics, vol. 8, 551 (1959).

9. P. C. Tandy, E. F. Redish, and D. Bollé, Physical Review Letters 35, 921 (1975).

10. P. C. Tandy, E. F. Redish, and D. Bollé, Physical Review C 16, 1924 (1977).

11. D. S. Koltun and D. M. Schneider, Physical Review Letters 42, 211 (1979).

12. M. S. Livingston, "LAMPF - A Nuclear Research Facility," LASL Report LA - 6878 - MS (1977).

13. G. S. Blanpied, "Scattering of 0.8 GeV Protons from ^{208}Pb, ^{12}C, and ^{13}C," LASL Report LA - 7262 - T (1978).

14. B. Zeidman, "The HRS Spectrometer System: Concepts and Design," LASL Report LA - 4773 - MS Part I (1971).

15. C. L. Morris, H. A. Thiessen, G. W. Hoffmann, IEEE Transactions on Nuclear Science, vol. NS-25, No. 1, pp 141-143 (1978).

16. F. Sauli, "Principles of Operation of Multiwire Proportional and Drift Chambers," CERN Publication 77 - 09 (1977).

17. "A Modular Instrumentation System for Data Handling," Euratom Report EUR - 4100e (1969).

18. B. Zacharov, "CAMAC Systems: A Pedestrian's Guide," Daresbury Nuclear Physics Laboratory, Daresbury, England (1972).

19. M. Kellogg, M. M. Minor, S. Schlaer, W. Spencer, R. F. Thomas Jr., and H. van der Beken, "Introduction to Q", LASL Report LA - 7001 - M (1978).

20. M. Kellogg et al., "QAL and the Analyzer Task", LASL Report LA - 6884 - M (1977).

21. R. J. Ridge, "DSP - A Histogram Display Program", unpublished (1979).

22. A. Wriekat et al., Physics Letters, to be published.

23. G. W. Hoffmann et al., Physical Review C 21, 1488 (1980).

24. R. E. Chrien et al., Physical Review C 21, 1014 (1980).

25. L. Ray et al., Physical Review C 23, 828 (1980).

26. L. Ray, University of Texas, Austin, Texas, unpublished.

27. G. S. Adams et al., Physical Review C 21, 2485 (1980).

28. P. V. Vavilov, JETP (USSR) 5, 749 (1957).

29. H. A. Bethe, Physical Review 89, 1256 (1953).

30. W. T. Scott, Reviews of Modern Physics 35, 231 (1963).

31. P. R. Bevington, Data Reduction and Error Analysis for the Physical Sciences, McGraw - Hill, N.Y. (1969).

32. J. Hudomalj - Gabitzsch et al., Physical Review C 18, 2666 (1978).

33. E. Ferrari and F. Selleri, Nuovo Cimento 21, 1028, (1961).

34. Günter Wolf, Physical Review 182, 1538 (1966).

35. L. Ray, Physical Review C 20, 1857 (1979).

36. Y. Alexander, J. W. van Orden, E. F. Redish, and S. J. Wallace, Physical Review Letters 44, 1579 (1980).